

NASA TECHNICAL NOTE




NASA TN D-2713

NASA TN D-2713

AMPTIAC

59733


DISTRIBUTION STATEMENT A
Approved for Public Release
Distribution Unlimited

**AERODYNAMIC DAMPING AND
BUFFET RESPONSE OF AN
AEROELASTIC MODEL OF THE
SATURN I BLOCK II LAUNCH VEHICLE**

by Perry W. Hanson and Robert V. Doggett, Jr.

*Langley Research Center
Langley Station, Hampton, Va.*

**Reproduced From
Best Available Copy**

AERODYNAMIC DAMPING AND BUFFET RESPONSE
OF AN AEROELASTIC MODEL OF THE SATURN I
BLOCK II LAUNCH VEHICLE

By Perry W. Hanson and Robert V. Doggett, Jr.

Langley Research Center
Langley Station, Hampton, Va.

NATIONAL AERONAUTICS AND SPACE ADMINISTRATION

AERODYNAMIC DAMPING AND BUFFET RESPONSE

OF AN AEROELASTIC MODEL OF THE SATURN I

BLOCK II LAUNCH VEHICLE

By Perry W. Hanson and Robert V. Doggett, Jr.
Langley Research Center

SUMMARY

A17-456 A17-457
The aerodynamic damping and buffet response of a flexibly mounted 0.08-scale aeroelastic model of the Saturn I Block II launch vehicle were measured at Mach numbers from 0.8 to 1.2. The basic configuration had for the payload an Apollo spacecraft with the launch escape system attached. The effects on the aerodynamic damping and bending-moment response of several modifications to the basic Apollo configuration were investigated. These modifications included the addition of a flow separator to the escape system rocket, removal of the first-stage fins, removal of the launch escape system from the Apollo spacecraft, substitution of a Jupiter nose cone for the Apollo spacecraft and escape system, and the substitution of some modified thin fins for the relatively thick wedge airfoil fins of the basic configuration. *La 222*

The experimentally determined values of aerodynamic damping in the flexible bending modes are compared with theoretical results. The model aerodynamic damping data and the buffet response data are scaled to full-scale values. *La 222*

INTRODUCTION

As launch vehicles become larger and more complex they must of necessity become structures of maximum design efficiency with a minimum of weight available for load carrying members. The resulting structures are relatively flexible so that the aerodynamics associated with the elastic deformations of these vehicles during the high-dynamic-pressure portion of their boost trajectories become quite important in determining the design requirements for stability and strength of the vehicles. The prediction of both aerodynamic damping and buffet response is important to the adequate determination of the loads that the vehicle will experience. A need exists for suitable theoretical approaches and experimental data on the oscillatory aerodynamic derivatives of flexible slender bodies of revolution characteristic of launch vehicles. Consequently, a research program has been undertaken to evaluate methods of handling these

20011130 132

structural dynamics problems, to provide a better understanding of the general nature of these problems, and to provide design information for selected specific vehicles.

The feasibility of using flexible models to provide experimental data on the oscillatory aerodynamic damping characteristics of slender flexible bodies was investigated and the results are reported in reference 1. The technique was refined and extended to launch vehicles that have much more complicated shapes, and the results of this investigation are presented in reference 2. The results of a parallel program to develop a method for determining directly the dynamic response of an aeroelastic launch-vehicle model to random (buffet) aerodynamic forces and to develop relationships useful in predicting full-scale vehicle response from model test results are presented in reference 3.

In the present investigation the experience derived from and the techniques developed in these earlier investigations have been applied to a 0.08-scale aeroelastic model of the Saturn I Block II launch vehicle. The purposes of this investigation were to determine whether or not significant destabilizing aerodynamic damping of the elastic bending modes would occur in the transonic Mach number range, and to obtain a measure of the buffet bending loads to be expected in flight. Three major configurations were investigated: a complete Saturn Apollo configuration, a Saturn-Apollo configuration without the launch escape system, and a Saturn-Jupiter configuration. Some minor changes in these basic configurations were also investigated. The investigation was conducted in the Langley transonic dynamics tunnel over the Mach number range from 0.8 to 1.2. The model was supported in such a manner that it was free to respond in simulated free-free bending modes and in the rigid-body pitch mode. The results of some theoretical approaches (refs. 4 and 5) are compared with the experimentally determined aerodynamic damping. Measured buffet and aerodynamic damping data are extrapolated to full-scale values.

SYMBOLS

C_a	generalized aerodynamic damping
C_c	full-scale control damping
C_{cr}	critical value of damping, $2M_S\omega$
C_h	damping derivative, $2\mu k \frac{C_a}{C_{cr}}$
C_s	structural damping
ΔC_s	increase in structural damping induced by electromagnetic damper
C_t	total damping

EI	bending stiffness
f	frequency of free-free bending mode, $\omega/2\pi$
f_θ	frequency of model rigid-body pitch mode
h	mode shapes based on unit nose deflection
k	reduced frequency, $2\pi fL/V$
L	length of configuration
M	free-stream Mach number
M_S	generalized structural mass, $\int_0^L m(x)h^2(x)dx$
m	mass per unit length
q	dynamic pressure, $\frac{1}{2}\rho V^2$
R	function defining model geometry, local radius
r	reference radius (radius of cylinder enclosing scalloped portion of model, 0.8575 ft)
V	free-stream velocity
W	total weight
x	longitudinal coordinate measured from rear of model
x_{cg}	longitudinal coordinate of center of gravity
α	angle of attack
μ	mass ratio, $\frac{M_S}{\pi \rho r^2 L \int_0^{L/r} \left[\frac{R(\frac{x}{r})}{r} \right] h^2(\frac{x}{r}) d(\frac{x}{r})}$ (derived in ref. 2)
ρ	fluid density
σ	root-mean-square bending moment
σ_Δ	root-mean-square bending moment with structural damping increased by ΔC_S

σ_t total root-mean-square bending moment, $\sqrt{\sigma_1^2 + \sigma_2^2 + \sigma_3^2}$
 ω circular frequency
 Subscripts:
 F full-scale vehicle properties
 M model properties
 n nth natural free-free bending mode, $n = 1, 2, 3, \dots$

APPARATUS AND PROCEDURE

Wind Tunnel

This investigation was conducted in the Langley transonic dynamics tunnel, which has a 16-foot-square test section (with cropped corners) and is a return-flow, variable-pressure, slotted-throat wind tunnel. It is capable of operation at stagnation pressures from about 1/4 lb/sq ft to slightly above atmospheric pressure and at Mach numbers up to 1.2. Mach number and dynamic pressure can be varied independently with either air or Freon-12 used as a test medium. Freon-12 was used in the present investigation. Stagnation temperature during the tests was approximately 125° F.

Model and Support System

General.- The basic model configuration investigated was a 0.08-size dynamically scaled aeroelastic model of a 2205-inch Saturn I Block II launch vehicle with an Apollo spacecraft and a launch escape system. The details of model geometry are presented in figure 1. In addition to the basic model configuration, six other geometrically different configurations were studied. These six were:

- (1) Basic configuration with flow separator.
- (2) Basic configuration without fins.
- (3) Basic configuration without launch escape system.
- (4) Basic configuration with Apollo nose replaced by Jupiter nose (this configuration will be referred to herein as the Jupiter configuration).
- (5) Jupiter configuration with basic fins replaced by modified (thin) fins (see fig. 1).
- (6) Jupiter configuration without fins.

Scaling.- The model was designed to simulate the full-scale vehicle mass ratio parameter μ (see symbol list) and reduced frequency k at $M = 1.00$ and $q = 615$ lb/sq ft. This corresponds to a model dynamic pressure of 265 lb/sq ft in freon. The scale factors used in model design were determined by wind-tunnel size and performance capabilities and by the full-scale trajectory flow conditions. (A detailed discussion of aeroelastic model scaling theory is presented in ref. 6.)

These scale factors were:

$$\frac{L_M}{L_F} = 0.08$$

$$\frac{W_M}{W_F} = 9.82 \times 10^{-4}$$

$$\frac{V_M}{V_F} = 0.476$$

$$\frac{m(x)_M}{m(x)_F} = 122.7 \times 10^{-4}$$

$$\frac{\rho_M}{\rho_F} = 1.918$$

$$\frac{(EI)_M}{(EI)_F} = 1.78 \times 10^{-5}$$

$$\frac{q_M}{q_F} = 0.435$$

$$\frac{f_M}{f_F} = 5.95$$

The model bending stiffness and weight distributions are compared with the desired full-scale values in figures 2 and 3, respectively.

The basic fin geometry, weights, and centers of gravity were scaled, but the fin stiffness distributions were not scaled.

Model construction.- Some of the details of model construction are shown in figure 4. Figure 4(a) shows in some detail the model fabrication concept. The structural backbone of the model was a central aluminum tube. Variation of the thickness and radius of the tube provided the properly scaled stiffness distribution except for minor deviations because of model structural considerations. Lead weights attached to the aluminum tube provided the proper weight distribution. The aluminum tube and lead weights were covered by segments of lightweight foam plastic which provided the correct external contour. Figure 4(b) shows a lead ring with the plastic shell attached. Figure 4(c) shows the segmented Jupiter nose cone and part of the central aluminum tube. The central aluminum tube was fabricated in sections to allow assembly onto the sting. The tube was integrally machined with raised rings spaced at intervals to stiffen the model in the radial plane and to provide strong mounting pads to receive the ballasted foam-plastic segments.

The basic fins were made of balsa wood covered with fiber glass. The modified fins were machined from aluminum.

In figure 4(d) two escape rocket assemblies are shown. The one on the right, called the truss escape rocket tower, was the original design. It was found in shake tests however that this tower was not strong enough to withstand the stresses imposed by the inertia loading when the model was forced to vibrate in its free-free bending modes. Another tower, the tube escape rocket tower, was fabricated in which a central titanium tube was machined to produce the same stiffness as that of the truss tower. The truss surrounding the tube was cut through so that it contributed no stiffness. The weight distribution was made to be the same as that of the truss tower. The tube tower was used throughout the tests except for a short check run with the truss tower in which it was determined that the use of the tube had no noticeable aerodynamic effect.

Figures 4(e) and 4(f) show the complete model mounted in the Langley transonic dynamics tunnel on the support system described in the next section.

Model support and excitation system.- The model was supported on a sting by means of a system of leaf springs, cables, pulleys, and torsion bars. Details of the support system are shown in figure 5. The support system was designed to restrain the model in the drag and yaw directions, support the model weight, provide a minimum of restraint to motion in the free-free bending modes, and simulate the full-scale control-system pitch stiffness at the Mach 1.0 design point on the boost trajectory. Figure 5(a) is a schematic diagram of the model support system used in this investigation, and figures 5(b) to 5(e) show photographic details of the system. The longitudinal leaf springs, attached to the inside of the structural tube of the model near the front and rear node points of the first free-free mode, restrained the model in the drag and yaw directions. They contributed approximately 25 percent of the pitch stiffness required to simulate the full-scale pitch frequency. The model weight was supported by cables (also attached to the model at the first free-free node points) reeved over pulleys on the sting and routed out the rear of the model to a system of torsion bars outside the test section. The torsion bars provided the remaining 75 percent of the required pitch stiffness. Incorporated in the downstream end of the rear leaf springs were transverse parallel springs designed to relieve midplane stresses generated in the longitudinal leaf springs by model rigid-body motions.

Since the point at which the model support cables left the sting translated down several inches as the angle of attack was increased from 0° , provision was made to automatically keep the tension in the cables constant. Before reaching the torsion bars, the model supporting cables were reeved over a sliding pulley block that was tied to the sting by a sting-movement sensing cable and to a piston in a constant-pressure pneumatic cylinder in such a manner that tension in the cables was kept constant as the angle of attack was increased. Thus, the model is free to pitch and translate, within limits, and to respond in essentially free-free bending modes. (See fig. 5(a).) Although the model is supported at the node points of the first free-free mode, this manner of support on springs that are soft relative to the model flexural stiffness provides a system that introduces negligible restraint even in the higher modes. (See, for instance, ref. 1.) A measure of the effects of the support system in the present investigation on the free-free bending modes may be made from the mode shape data presented in figure 6. As is seen from the

figure the agreement between the experimental data measured with the model mounted on the support system and the theoretical calculations, which did not take into account the support system, is good. Therefore, the effects of the support system are assumed to be small.

Other features and details of the support and excitation system are shown in the photographs of figure 5. The electromagnetic shaker which was used to excite the model in its elastic bending modes of vibration in order to determine the aerodynamic damping in each mode is shown in figure 5(b). The field coils were attached to the sting and the moving coils were attached to the inside rear of the model. A cooling water jacket was provided to keep the temperature of the field coils within acceptable limits. Shown in figures 5(b) and 5(c) are the pneumatically operated model "snubbers," which were used to hold the model rigidly to the sting when tests were not being made and to provide a means of restraining model rigid-body motions should an instability be encountered. Switches under the snubbers indicated whether or not the snubbers were fully retracted. Switches on the sting at points where the model could contact the sting indicated if the model was striking the sting. A fouling indicator was also incorporated in the shaker to show that the moving coils were riding freely. Electrical resistance strain gages on the leaf springs also indicated the model position with respect to the sting.

Figure 5(d) shows an overall view of the sting and support cables internal to the model. As the support cables on each side of the model left the rear of the model, each pair was tied together by whiffle-tree arrangement and then routed up the front of the sting support strut to the plenum chamber on top of the test chamber. The cables were shielded from the air flow by the shields shown in figures 4(e) and 4(f).

Figure 5(e) shows the portion of the support system that was external to the test section. The cables from the model pass over the pulleys in the sliding pulley block and are attached to the torsion bar lever arms. There is a torsion bar for the front upper cable, which supports the forward portion of the model, and one for the front lower cable, which opposes (preloads) the front upper cable. There is a similar arrangement for the rear cables. The stiffness levels of the front and rear torsion bars are such that the model will pitch about its center of gravity at the scaled pitch frequency of the full-scale vehicle.

The ends of the torsion bars opposite the lever arms are held in clamps which can be independently rotated by electric drive motors controlled from the wind-tunnel control room. Thus, at an angle of attack when the lift forces tended to raise the model with respect to the sting, the model could be kept centered on the sting as indicated by the leaf spring strain gages.

Model physical properties.- The physical properties of the models are presented in table 1 and figure 6.

Lead ballast was used in conjunction with the removal of the basic fins and the substitution of the modified fins. Consequently, the weight distributions, mode shapes, and frequencies of the Jupiter configurations with and

without the basic fins and with the modified fins were the same. Similarly, these parameters were the same for the Apollo configurations with and without fins. The weight of the flow separator was negligible so that there was no measurable difference in the weight distribution, mode shapes, and frequencies of the basic Apollo configuration and the Apollo configuration with the flow separator.

The generalized masses given in table 1 were experimentally determined by using the incremental mass method of reference 7. The experimental mode shapes were determined by forcing the model with the electromagnetic shaker at the resonant frequency and by measuring the variation along the model of the relative vertical displacement by means of a small accelerometer. The model was also checked to make certain that no portion was responding in extraneous radial modes. Calculated mode shapes are also shown in figure 6. The agreement between the calculated free-free mode shapes and the mode shapes actually measured on the model mounted on the support system is considered to be very good, and indicates that the free-free modes were not unduly influenced by the mounting system. The first three free-free bending modes of the Saturn-Apollo configuration and the first two bending modes of the Saturn-Apollo configuration without escape system and of the Saturn-Jupiter configuration are shown. For the third bending mode, with either the Jupiter nose cone or the Apollo configuration with escape system off, portions of the cable suspension system resonated. This resonance had the effect of absorbing a large amount of the power available from the shaker so that the model could not be excited to a reasonable amplitude. Therefore, no data are presented for the third bending mode of these two configurations. However, the third-mode frequency for both the Apollo configuration without escape system and the Jupiter nose cone configuration was about 50 cps.

Instrumentation

The instrumentation used in this investigation is shown schematically in figure 7. The dynamic bending moments were indicated by suitably calibrated four-active-arm resistance-wire strain-gage bridges bonded to the central aluminum tube. Several of these gages became inoperative during the tests. The data from one gage that worked throughout the investigation and was sensitive to bending strains for all modes of interest for all the configurations were selected for analysis. The electrical center of this gage was located at model station 73.5 inches.

A quartz accelerometer was located at the point of application of the shaker force to the model (model station 6.67 inches). The accelerometer output signal was used in conjunction with the shaker force output (determined from shaker armature current) to determine the aerodynamic damping by means of an electronic transfer function analyzer. Accelerations at several other stations were sensed by unbonded-strain-gage accelerometers. These accelerometers were used to monitor model amplitude.

In order to minimize the possibility of inadvertently shaking the model at amplitudes that would impose greater than design stresses, an accelerometer

at the rear of the model was used to actuate a switch to cut power from the shaker when the acceleration reached a predetermined maximum level for each vibration mode.

Several pressure transducers were located in the model upper stages in an attempt to measure oscillating pressures as a secondary experiment. Most of these gages became inoperative early in the tests. The data from the remaining gages require further analysis and are not reported herein.

Resistance-wire strain-gage bridges mounted on the four leaf springs were used to indicate when the model was centered on the sting. No data were recorded from these bridges.

Temperatures of the model skin, the central aluminum tube, the shaker field coils, and the shaker moving coils were sensed by thermocouples.

Microswitches were placed under the snubbers on the sting to indicate whether or not they were fully retracted during the portions of the test when data were being taken. Microswitches were also placed at points on the sting where the model could possibly contact the sting during large-amplitude rigid-body motions.

A fouling indicator was incorporated in the shaker to show whether or not the moving armature coils (attached to the model) were clear of the field poles (attached to the sting).

The signals from all the unbonded strain-gage accelerometers, bending-moment strain gages, and pressure cells were amplified by 3-kc carrier amplifiers. The amplified signals were recorded on an oscillograph and on a 14-channel tape recorder. These signals also went to a switch box which allowed any desired signal to be monitored. During part of the investigation (first series; see section entitled "Test Procedure"), the signal to be monitored was switched through a 600-cps low-pass filter, through a linear amplifier which was used to reject any dc bias that was present in the signal, and through an amplifier to a thermocouple voltmeter. The ac signal from the model displayed on the thermocouple voltmeter was observed for a period of time and an average value of the meter reading was recorded. Since at times the fluctuations in the indicated signals were quite large, the need for a system that would provide for a more consistent averaging of the fluctuating mean-square signals was evident. Therefore, for the second test series a signal integrating scheme was employed. After leaving the 600-cps low-pass filter, the fluctuating signal was sent through a mean-square amplifier, to an electronic integrator. The integrated signal was displayed continuously on a dc voltmeter. When the integrating period was completed, the integrated value remained displayed on the voltmeter until released. The integrator was calibrated so that the integrated reading could be interpreted in terms of the average root-mean-square value of the signal. This system allowed for reliable, rapid comparison of the response of the various configurations to the tunnel flow conditions. The root-mean-square values recorded in this manner during the investigation were later compared with those obtained from electronic analysis

of the magnetically taped signals and were found to agree very well. The integrated data recorded during the tests were used in the determination of the buffet bending moments.

The signal being monitored could also be sent to an oscilloscope and to an electronic damping meter (see ref. 8), which measured the logarithmic decrement of the signal, and was used to monitor the model structural damping to determine any large changes due to structural failure. The accurate measurement of damping requires a fairly "clean" decaying signal; therefore, the damping meter could not be used under most "wind-on" conditions.

In addition to the described monitoring circuit, any one of four preselected signals could be monitored on a true-root-mean-square vacuum-tube voltmeter as a guide to the operator of the electrodynamic shaker in the setting of the model vibration amplitude for the determination of damping.

The shaker armature was driven by the output of a 1,000-volt-ampere power amplifier, and the field coil was excited by a 250-volt, 40-ampere dc power supply. A variable-frequency oscillator provided the input signal to the ac power amplifier through a servoamplifier, which was a variable-gain unit; the gain was controlled by a signal from the output current of the power amplifier. The effect of the servoamplifier was to hold the output current (and therefore the shaker force) constant in spite of varying back electromotive force generated by airflow-induced movements of the model in the tunnel. This is a necessary requisite to the use of the "power method" of determining aerodynamic damping. (See ref. 1.) Unfortunately, within the power range of most of this investigation this feature was not effective; therefore, no aerodynamic damping data obtained by the power method are presented.

A variable-phase oscillator installed as part of the transfer-function analyzer was used to drive the shaker-armature power amplifier. As the model responded to input forces, signals proportional to the shaker armature current and to the output of the quartz accelerometer (located at the point of application of the shaker force) were fed into the transfer function analyzer. The analyzer resolved the armature current (proportional to the shaker force) and the accelerometer output signal into in-phase and quadrature components with reference to the oscillator output. A servo control automatically shifted the oscillator output phase to be in phase with the current. The resulting acceleration and force components were digitized by millivolt readers and tabulated by an electronic printer. These data were used to determine the aerodynamic damping results presented in this report.

Test Procedure

With the model mounted in the tunnel and no air flowing (but with the model temperature approximately the wind-on value), the electromagnetic shaker was used to excite the model at the resonant frequencies of its free-free bending modes at several pressures from atmospheric pressure down to moderately low pressures. The model was excited to an amplitude that would be the same as that during the wind-on portion of the test since previous calibrations had

shown the model structural damping to be somewhat amplitude-dependent. No change in resonant frequency or damping was observed for these various tunnel pressure conditions.

In each mode, while the model was vibrating at a given amplitude, the shaker force and acceleration data necessary for application of the transfer-function-analyzer method of determining damping were recorded. The power to the shaker was then abruptly shut off (and the shaker moving coils disconnected from the electrical circuit while the current to the field coils was also shut off), the decaying oscillations of the model were recorded, and the logarithmic decrement was measured by the electronic damping meter. This device provided a quick means of detecting any changes in structural damping due to structural failure, loose screws, binding cables, and so forth. Damping measurements were also made during free decay with the shaker moving coils in the electric circuit (but not being driven) and with varying amounts of current applied to the field coils. Under these conditions, the electromagnetic shaker became a damper; thus, for a given field current, the model structural damping was increased by a known amount. This information was needed for an investigation to determine the effect of changes in structural damping on the model response to buffet flow.

After obtaining the no-wind data, the model snubbers were extended and the tunnel started. When the tunnel reached the desired operating conditions, the snubbers were retracted and the response of the model was observed. The tunnel was operated throughout the Mach number test range to ascertain that no dynamic instabilities existed. The wind-on data needed to measure the aerodynamic damping were then obtained in the following manner. The tunnel was brought to a desired Mach number, and the model was forced to vibrate at each of its free-free resonant frequencies. The total damping data were recorded (except that the decaying oscillations no longer produced a signal that was clean enough in most cases to permit use of damping meter) in the same manner as was done under no-wind conditions. As in references 1 and 2, attempts were made to measure aerodynamic stiffness, but no discernible change in model frequency was apparent other than the normal scatter in the data between wind-off and wind-on tunnel conditions. Wind-on frequency determination was accurate to about 1 percent. Once the damping data were recorded, the buffet response data were obtained by setting the shaker armature coils open (with no current to the field coils) and by allowing the model to freely respond to the flow conditions while approximately 45 seconds of data from the model transducers were recorded on tape. During this time, the root-mean-square values of signals from selected bending-moment strain gages were recorded (either from the thermocouple voltmeter or from the integrator circuit dc voltmeter). The process was continued at the various Mach numbers, dynamic pressures, and angles of attack for all the configurations investigated.

Two series of investigations were conducted. The purposes of the first series were to determine whether or not significant destabilizing aerodynamic damping of the elastic bending modes would occur in the transonic Mach number range and to obtain a measure of the buffet bending loads to be expected in flight. Investigated in this first series were the basic Apollo configuration

with and without the flow separator on the escape rocket, basic Apollo configuration without the escape system, and the basic Jupiter configuration.

The purposes of the second series were to attempt to obtain more definitive data on the configurations of the first series at the Mach numbers of greatest interest and to investigate the effects of removing the basic fins from the basic Apollo and Jupiter configurations, and of substituting fins on the Jupiter configuration which had the same planform but a much thinner airfoil (NACA 65A003) than the wedge airfoil of the basic fins (which had a thickness-chord ratio of 0.1).

The Reynolds number per foot ranged from 1.0×10^6 to 4.2×10^6 . Most of the data were obtained at 3.9×10^6 .

DATA ANALYSIS

Aerodynamic Damping

It is well known that at resonance the damping of a single-degree-of-freedom system is equal to the applied force divided by the velocity of application of the force. For a particular mode of a continuous system the damping at resonance is equal to the applied generalized force divided by the velocity of the generalized coordinate. For conditions other than at resonance the damping (viscous type) is equal to the applied generalized force divided by that component of the velocity of the generalized coordinate that is 180° out of phase with the applied force. For this investigation the applied force was obtained from the shaker armature current. (For a given field coil current, the shaker output force was proportional to the armature current.) The velocity was obtained from measurements of the acceleration. Since the model was driven in simple harmonic motion, the velocity could be determined by division of the acceleration by the circular frequency. It should be pointed out that the basic concepts used in determining the damping in this investigation are the same as those of reference 1. The current to the moving coils and the acceleration were determined by means of the electronic transfer function analyzer. The

model aerodynamic damping ratio $\left(\frac{C_a}{C_{cr}}\right)_M$ was determined by measuring the total damping with the wind on and subtracting from that value the structural damping ratio determined with the wind off.

A nondimensional damping-force derivative that is useful in scaling model aerodynamic damping results to equivalent full-scale conditions can be defined in terms of the usual flutter parameters, reduced frequency and mass ratio, in such a manner as to permit estimation of aerodynamic damping of similar configurations having somewhat different structural characteristics. Thus, from reference 2

$$C_h = 2k\mu \frac{C_a}{C_{cr}} \quad (1)$$

In equation (1), k , the reduced frequency, is defined as $\frac{2\pi f L}{V}$ and μ , an

effective mass ratio, is defined as $\frac{M_s}{\pi \rho r^2 L \int_0^{L/r} \left[\frac{R(\frac{x}{r})}{r} \right] h^2(\frac{x}{r}) d(\frac{x}{r})}$ where

$\int_0^{L/r} \left[\frac{R(\frac{x}{r})}{r} \right] h^2(\frac{x}{r}) d(\frac{x}{r})$ is a weighting function with respect to the body shape

and the square of the mode shape. It is believed that this is a more logical definition of the mass ratio μ than the more conventional definition, since the numerator is the generalized mass (which contains the square of the mode shape) instead of the physical mass of the system. The values of the integral for the various configurations investigated are given in table 1.

Buffet Bending Moments

In order to predict the magnitude of full-scale buffet loads from investigations of dynamically scaled aeroelastic models, it is necessary to determine the proper scaling relationships for such a system. A dynamic analysis of launch-vehicle buffeting has been considered in some detail in reference 3. In the analysis, based on simple beam theory and the techniques of generalized harmonic analysis (which is treated in some length in ref. 9 and was first applied to the analysis of buffeting in ref. 10), the vehicle was assumed to be flying at constant altitude with a constant velocity. The only aerodynamic forces present in addition to the random component were damping forces proportional to the velocity of the bending vibrations of the system. No loss of generality results from neglecting the aerodynamic inertia and spring forces since such forces usually are small when compared with their structural counterparts for a slender launch vehicle. (See, for instance, refs. 1 and 2.) Structurally, the vehicle was considered to be a linear multidegree-of-freedom system. The final result obtained from this analysis for the total full-scale root-mean-square bending moment at some longitudinal station x is

$$\sigma_{t,F}(x) = \sqrt{\sum_{n=1}^{\infty} \left(\frac{I_F}{I_M} \right)^7 \left(\frac{f_{n,F}}{f_{n,M}} \right) \left(\frac{q_F}{q_M} \right)^2 \left(\frac{V_M}{V_F} \right) \left[\frac{\left(\frac{C_a}{C_{cr}} \right)_{n,M} + \left(\frac{C_s}{C_{cr}} \right)_{n,M}}{\left(\frac{C_a}{C_{cr}} \right)_{n,F} + \left(\frac{C_s}{C_{cr}} \right)_{n,F} + \left(\frac{C_c}{C_{cr}} \right)_{n,F}} \right] [\sigma_{n,M}(x)]^2} \quad (2)$$

where $\left(\frac{C_a}{C_{cr}} \right)_F$ can be obtained from the relation

$$\left(\frac{C_a}{C_{cr}}\right)_{n,F} = \frac{C_{h,n}^*}{2k_{n,F} \mu_{n,F}} \quad (3)$$

or from the relation

$$\left(\frac{C_a}{C_{cr}}\right)_{n,F} = \left[\left(\frac{\rho_F}{\rho_M}\right) \left(\frac{V_F}{V_M}\right) \left(\frac{L_F}{L_M}\right)^2 \left(\frac{W_M}{W_F}\right) \left(\frac{f_{n,M}}{f_{n,F}}\right) \right] \left(\frac{C_a}{C_{cr}}\right)_{n,M} \quad (4)$$

and $\left(\frac{C_s}{C_{cr}}\right)_{n,F}$ is the full-scale structural damping ratio, $\left(\frac{C_c}{C_{cr}}\right)_{n,F}$ is the full-scale control-system damping ratio, and $\sigma_{n,M}(x)$ is the model root-mean-square bending moment in a given mode at a particular longitudinal station on the model.

It can be seen that the total mean-square bending moment is a superposition of single-degree-of-freedom results (coupling terms were neglected in the derivation), each mode being independently treated as a separate system. Thus, aside from the flow conditions, the model parameters to be measured in each free-free bending mode of interest are the model structural and aerodynamic damping and the buffet bending-moment response. (Although eq. (2) has been developed for bending-moment response, it should be pointed out that expressions similar to eq. (2) could be obtained for any response quantity which is proportional to displacement.) The various full-scale trajectory flow conditions and full-scale structural and control-system damping used in this report to scale model results to full-scale values are shown in table 2. The data given in the table are based on the following assumptions:

(1) Full-scale dynamic pressure, density, velocity, and vehicle weight for the basic Apollo configuration are typical of 100-nautical-mile-orbit boost trajectories. The same trajectory dynamic pressure, density, and velocity are used for all configurations.

(2) It is assumed that at $M = 1.0$ the basic Apollo configuration without escape system and the Jupiter configuration scale exactly their full-scale counterparts. The changes in full-scale weight W_F along the trajectory from the $M = 1.0$ point for these configurations are assumed to be the same as for the basic Saturn-Apollo vehicle.

(3) It is assumed that at $M = 1.0$ all model configurations exactly scale actual-launch-vehicle frequencies and generalized masses. Full-scale frequencies along the trajectory at other than $M = 1.0$ are assumed to be inversely proportional to the square root of the ratio of the total weight at a point to the weight at $M = 1.0$. The full-scale generalized mass $M_{s,F}$ along the trajectory from the $M = 1.0$ point is assumed to vary directly with the vehicle weight (no change in mode shape).

(4) The control damping ratios for the basic Apollo and Jupiter configurations were obtained from unpublished data obtained from the NASA Marshall Space Flight Center. Control damping ratios for the Jupiter configuration are assumed to be applicable to the Apollo configuration without the launch escape system.

(5) The full-scale structural damping ratios of the basic Apollo and Jupiter configurations are values that were measured on the full-scale shake-test vehicles. (See ref. 11.) Structural damping of the Apollo configuration without the escape system is assumed to be the same as that of the basic Jupiter configuration.

Since, in practice, the buffet response of the model is measured at some point on the model in terms of the total bending-moment response rather than the bending moment due to model response in a given vibration mode, in order to scale the model results to full-scale values by using equation (2), it is first necessary to determine the relative contribution of each natural mode to the total bending moment measured on the model at a particular location. This determination can be accomplished by integrating the power spectra in the neighborhood of the resonant frequency of the desired mode. Some of the data recorded on magnetic tape were reduced to power spectral densities by the use of an electronic analog analyzer over the frequency range from 0 to 50 cps by using a 0.5-cps bandwidth filter. Sample bending-moment power spectra for the major configurations investigated are shown in figure 8. (The apparent discrepancies between the frequencies of maximum response and the indicated resonant frequencies are due to a bias in the fine tuning of the analyzer.) Note that for the basic Apollo configuration, although the response was primarily in the first mode, there was some response in the second and third modes whereas, for the Apollo configuration without the escape system and for the Jupiter configuration, the contribution of the second mode to the total response was quite small and no contribution of the third mode was apparent.

Although the full-scale bending moment at a particular location along the vehicle can be determined directly from equation (2), the missile or launch-vehicle designer needs to know the distribution of bending moments along the structure. Therefore, a strain-gage-location sensitivity factor must be determined, since a bridge located at the point of maximum bending moment in the first mode may not be very sensitive to moments produced by response in the second mode. This factor can be determined by calculating the bending-moment distribution due to inertia loading for motion in each mode, respectively. The resulting bending-moment distributions for the configurations investigated are shown in figure 9. Also shown are comparisons of some bending moments actually measured (while the model was forced to vibrate at resonance with wind off) and the calculated values at the point of measurement.

Once the full-scale buffet bending-moment distribution in each mode was determined, the mean-square buffet bending moments at each station for the various modes were then added to obtain the total bending-moment distributions.

RESULTS AND DISCUSSION

Aerodynamic Damping

The results of the aerodynamic damping portion of the investigation are shown in figures 10 to 12. In figure 10 the results are presented in terms of the variation of the aerodynamic damping derivative C_h with Mach number for zero angle of attack. Figure 10(a) shows the effect of the removal of the fins from the basic Apollo configuration (no flow separator) on the aerodynamic damping derivative. (Full-scale damping ratio is obtained by dividing the damping derivative C_h by $2\rho_F k_F$.) The effect was a slight lowering of the damping primarily in the first bending mode. The effect on the second- and third-mode aerodynamic damping is not as readily apparent because of the scatter in the experimental data. The calculated values, from reference 4, of aerodynamic damping for the basic Apollo configuration agree very well with measured values for the first mode, and for the second mode at the lower Mach numbers. The calculated values for the third mode were generally lower than those measured. A quasi-steady approach is used in reference 4, which attempts to account for the effects of separated flow on the aerodynamic damping. Damping derivatives calculated from momentum theory (see ref. 5, for instance) were low for all modes and, of course, except for the effect of the fins (which was obtained from quasi-steady calculations based on unpublished experimental normal-force data), show no Mach number effect.

A comparison of the data in figures 10(a) and 10(b) shows the effect of adding the flow separator to the basic Apollo configuration. Aerodynamic damping measured with the flow separator on the escape rocket was generally less than that measured without the flow separator for the first two bending modes. No discernible effect was noted for the third mode. Once again the calculated values of damping of reference 4 agree well with the measured values for the first two modes but do not agree with the measured damping in the third mode. The calculated values obtained from momentum theory on the body and from a semi-empirical approach for the fins are representative of an average damping in the second mode over the Mach number range investigated and also at the lower Mach numbers in the first mode.

Figure 10(c) shows the effect of removing the launch escape system from the basic Apollo configuration. The aerodynamic damping for this configuration was in general larger than that for the other Apollo configurations for the first two vibration modes. An increase in damping was predicted by both the analytical approach of reference 4 and that of reference 5.

Figure 10(d) shows the effects on the aerodynamic damping of replacing the Apollo nose with a Jupiter nose, the effects of removing the basic fins from the Jupiter configuration, and the effects of replacing the thick-wedge-airfoil basic fins with modified fins, that had the same planform but which had a thin NACA 65A003 airfoil. Although there is considerable scatter in the data, some general conclusions may be drawn. The subsonic aerodynamic damping in the first mode was increased slightly for the basic Jupiter configuration over that of the Apollo configuration without the escape system. Little effect

was noted in the supersonic Mach number range. A comparison of the aerodynamic damping in the second modes of the two configurations reveals that the undulating character of the variation of damping with Mach number of the Apollo configuration without the escape system is not apparent for the Jupiter configuration.

The removal of the basic fins from the Jupiter configuration resulted in a large decrease in aerodynamic damping in both the first and second bending modes over the Mach number range investigated. Substitution of the modified (thin) fins for the basic fins resulted in aerodynamic damping that was intermediate to the damping of the configurations with and without the basic fins.

The aerodynamic damping values calculated from momentum theory on the body and from empirical data on the fins are generally low for both the first and second modes of the Jupiter configuration with the basic fins. Removal of the fins resulted in a greater decrease in damping than indicated by momentum theory for both the first and second modes.

The effects of changes in angle of attack on the variation of the damping derivative at Mach 0.9 are shown in figure 11. Figure 11(a) presents the results for the various modifications to the Apollo configuration with the escape system. Generally, angle-of-attack variations had little effect on the aerodynamic damping derivative. Removal of the fins from the basic Apollo configuration resulted in a decrease in damping for all angles of attack investigated in the first and third modes but little effect on damping in the second mode. The damping levels of the first and third modes were also decreased when the flow separator was added to the escape rocket of the basic Apollo configuration.

Figure 11(b) shows the effect of removing the escape system from the basic Apollo configuration. A much larger variation of aerodynamic damping with angle of attack is apparent.

Figure 11(c) shows that substitution of the Jupiter nose for the Apollo nose resulted in a decrease in damping except at zero angle of attack. Removal of the fins from the basic Jupiter configuration resulted in a further decrease in damping even to the extent that the aerodynamic damping became negative (destabilizing) at angles of attack of 2° , 4° , and 6° in the second mode. During the first test series negative damping was also measured at an angle of attack of 6° in the second mode of the basic Jupiter configuration (with basic fins). However, this data point was not repeated in the second test. Substitution of the modified (thin) fins for the basic (thick) fins had little effect on the variation of aerodynamic damping with angle of attack.

Averaged values of the damping derivative C_h have been used with full-scale mass ratios and reduced frequencies (calculated from the trajectory data in table 2) to obtain the variation of the full-scale aerodynamic damping ratio $(C_a/C_{cr})_F$ with flight time shown in figure 12 for the basic Apollo and basic Jupiter configurations at zero angle of attack. The solid portion of the curves represents the range of the wind-tunnel studies on the model ($M = 0.8$

to $M = 1.2$). The dashed portions of the curves are estimated values. The peaks at $M = 1.2$ are caused primarily by the parameter ρV which diminishes rapidly after about 60 seconds of flight. The maximum values of full-scale aerodynamic damping measured on the basic Apollo configuration are only about 20, 60, and 50 percent of the estimated sum of the full-scale structural and control-system damping in the first, second, and third flexible bending modes, respectively. (See table 2.) The maximum aerodynamic damping in the first mode of the Jupiter configuration is about 30 percent of the total structural and control-system damping and about 60 percent in the second mode.

Bending-Moment Response

The results of that portion of the investigation concerned primarily with buffet bending-moment response are shown in figures 13 to 16. The effects on model bending-moment response of variations of configuration, angle of attack, and structural damping will be considered first. The results will be interpreted subsequently in terms of full-scale values. Figure 13 presents the effect of configuration changes on the variation of model root-mean-square bending moment (measured at model station 73.5 inches) with Mach number at an angle of attack of 0° . From figure 13(a), which presents data on Apollo configurations with the escape system, several observations can be made.

Since the model bending-moment response is a function of dynamic pressure q , variations in this parameter were generally held within the range of 225 to 250 lb/sq ft with most of the tests being conducted at about 235 lb/sq ft. However, one run was made at dynamic pressures of about 150 to 170 lb/sq ft. For cases where aerodynamic damping is large relative to structural damping, the dynamic analysis of reference 3 (from which the scaling relationship, eq. (2), is derived) shows that the structural response to a random input varies with the square root of the dynamic pressure. The model bending-moment responses at these low levels of dynamic pressure have been adjusted to values that would be associated with the higher levels of dynamic pressure by multiplying the bending moment at the lower level by the square root of the ratio of the higher dynamic pressure to the lower dynamic pressure. These data points are shown in figure 13(a) by the solid circles. These adjusted values agree very well with the bending moments measured at the higher levels of dynamic pressure.

The addition of the flow separator to the basic Apollo configuration caused a slight increase in model bending moment at all test Mach numbers except at Mach 0.8.

When the fins were removed from the basic Apollo configuration, lower bending moments were experienced by the model throughout the Mach number range. Unfortunately, because of a failure in the tunnel Mach number indicator that was not detected during the investigation, the peak response for this configuration was not determined.

A final observation to be made from figure 13(a) is that the data measured during both test series agree very well.

Figure 13(b) shows the bending-moment response variation with Mach number when the escape system (tower and rocket) was removed from the basic Apollo configuration. The reader is cautioned against comparing the magnitude of the bending-moment response of this configuration with that of the basic Apollo configuration, since removal of the escape system resulted in a significant change in mode shapes and bending-moment distributions.

Figure 13(c) presents the results of some modifications to the Jupiter configuration. The character of the bending-moment response of the basic Jupiter configuration differs in some respects from that of the Apollo configuration. The maximum response occurs at a slightly lower Mach number, and the decrease in response after the peak is more rapid than that of the Apollo configurations. Removal of the fins from the basic Jupiter nose cone configuration resulted in a decrease in model bending moments in the vicinity of the peak response, but just the opposite effect is observed at Mach numbers 0.8 and 0.92. Removal of the relatively thick basic fins would of course remove any buffet input to the model due to these fins, but their removal also results in a loss of some aerodynamic damping, which would account for the increase in model response outside the buffet Mach number range. When the basic (thick) fins were replaced with the modified fins, the model response was generally between that of the basic configuration and the no-fin configuration. The conclusion is that the thick basic fins generated some buffet flow that contributed to the overall model response.

The effects of angle of attack on the variation of model total root-mean-square bending moment at station 73.5 inches for the various configurations investigated are shown in figure 14. The buffet bending-moment responses of the Apollo configurations are presented in figure 14(a). At Mach 0.8 there was only a slight increase in bending moment with angle of attack for the basic Apollo configuration whereas at Mach 0.9 there is a large increase in response with an increase in angle of attack, for both the basic Apollo configuration and the Apollo configuration without the fins. Removal of the fins had the effect of reducing the bending moment experienced by the model throughout the angle-of-attack range. Removal of the escape system from the basic Apollo configuration resulted in a change in the character of the variation of bending moment with angle of attack with the maximum measured bending moment occurring at an angle of attack of 3° . Once again, the magnitude of the model bending moment of the Apollo configuration without the escape system relative to that of the basic Apollo configuration is of no significance because of the differences in mode shapes and bending-moment strain-gage-location sensitivity factors of the two configurations. As a matter of fact, the mode shapes, power spectra, and strain-gage-location sensitivity factors for the Apollo configuration without the escape system are nearly the same as those for the Jupiter configuration. (See figs. 6, 8, and 9.)

Figure 14(b) presents the effects on the model root-mean-square bending moment of variations in angle of attack at a Mach number of approximately 0.9 for the various Jupiter configurations studied. The bending-moment response of the basic Jupiter configuration increases with an increase in angle of attack although not as sharply as that of basic Apollo configuration. Removal of the fins from the basic Jupiter configuration resulted in a large decrease

in bending-moment response. When the thick wedge-shaped basic fins were replaced by fins that were less than one-third as thick and had a more conventional airfoil shape, the root-mean-square bending moment experienced by the model was reduced by 25 to 35 percent, and there was little increase in bending-moment response with increasing angle of attack up to 4° .

Since one would not expect buffet flow over a slender cone (as the Jupiter nose cone), it is believed that the bending-moment response of the basic Jupiter configuration must have been due to buffet input from other regions of the vehicle and to turbulence in the tunnel flow. Of course, nothing could be done about the tunnel turbulence, but it is believed that the relatively thick fins on the basic Jupiter configuration could very well be one source of buffet input to the vehicle. Also, any fins could very well amplify the effects of tunnel turbulence. The following interpretation could be placed on the results of the fin investigation. The bending-moment response of the Jupiter configuration without fins at the lower angles of attack could be primarily due to tunnel turbulence and, perhaps, some buffet input from regions of the vehicle other than the nose or fins - for instance, the relatively steep flare that separates the scalloped first stage from the cylindrical second stage. The increase in bending-moment response brought about by the addition of the relatively thin fins could be attributed to an amplifying effect of the fins on the tunnel turbulence. That is, the fins provide an added source of lift forces acting on the model because of small angle-of-attack fluctuations due to tunnel turbulence.

The further increase in model bending-moment response when the thin fins were replaced by the relatively thick, wedge-shaped fins of the basic configuration can be attributed to buffeting flow over these fins. The use of the response of the Jupiter configuration with modified fins as a "tare" value of response due to tunnel turbulence to be subtracted from the total response of other configurations to obtain the model response due to buffeting only is an appealing concept. Any such correction would have to be on a modal basis and, unfortunately for the present investigation, the differences in the mode shapes and power spectra of the Apollo and Jupiter configurations preclude this simple approach. However, as mentioned previously, the mode shapes, power spectra, and strain-gage sensitivity factors of the Apollo configuration without the escape system are about the same as those of the Jupiter configuration; and since nearly all the model response was in the first bending mode for both configurations, an estimate may be made of that portion of the bending-moment response of the Apollo configuration without the escape system that was due to buffeting, if the assumption is made that there is no correlation between tunnel turbulence and the buffet flow. Thus, a comparison of the bending-moment response of the Jupiter configuration with modified fins (fig. 14(b)) with the response of the Apollo configuration without the escape system (fig. 14(a)) shows that buffet flow over the relatively blunt nose of the Apollo configuration accounts for approximately one-third of the total response at angles of attack of 0° and 6° and for about one-half at 3° .

Another factor which influences the bending moments experienced by a vehicle in buffet flow is the total vehicle damping. Equation (2) indicates that the root-mean-square bending-moment response is inversely proportional to the

square root of the total damping. An attempt was made to verify this relationship by increasing the model structural-damping portion of the total damping and by measuring the corresponding bending-moment response of the model. As mentioned previously, this variation in structural damping was accomplished by using the electromagnetic shaker as a variable damper. The results are shown in figure 15. The ordinate is the ratio of model root-mean-square bending moment with increased structural damping to the root-mean-square bending moment with original damping. The abscissa is the square root of the total-damping ratio. (The variation is due to increments in structural damping.) The solid line represents the variation of bending moment with the inverse of the square root of the total-damping ratio. The symbols are measured model data. The response of the basic Jupiter configuration in the first mode is shown for several levels of total damping. (Nearly all the response of this configuration was in the first mode. See fig. 8(c).) The response of the basic Apollo configuration in each of its first three free-free modes is shown for one value of increased total damping in each mode. The variation of model bending-moment response with total damping agrees very well with that indicated by equation (2).

The results presented in figure 13 show that all model configurations experienced a peak response in the vicinity of a Mach number of 0.9. The peak-response model data were selected for scaling to full-scale values for the two actual flight configurations - the basic Apollo configuration (without flow separator) and the basic Jupiter nose cone configuration. These predicted maximum full-scale root-mean-square bending-moment distributions are shown in figure 16 for angles of attack of 0° and 6° . The data are for the Mach 0.9 point on the vehicle boost trajectory. In addition to the total full-scale bending-moment distributions shown for angles of attack of 0° and 6° , the full-scale bending-moment contribution of the first mode only is shown for an angle of attack of 0° . The effect of the higher modes on the bending-moment distribution is evident, particularly for the Apollo configuration. The total full-scale root-mean-square bending moments shown can be regarded as the maximum likely to be experienced due to buffeting, since some response to tunnel turbulence is inherent in these extrapolated full-scale values. Further investigations are needed to determine a valid approach for separating the effects of tunnel turbulence from the total measured model response.

One factor of importance that has a bearing on the validity of the extrapolated full-scale bending-moment response is the accuracy with which the degree of the contribution of the various modes to the total response can be determined. The larger the contribution of the higher modes, the more important this factor becomes. An analysis of the data from the present investigation indicated that the taped samples of model bending-moment response (45 to 60 seconds) were not sufficiently long to produce a completely repeatable power spectra for a given constant flow condition. However, an engineering evaluation of all the power spectra at the Mach number of greatest response (approximately Mach 0.9) allowed a determination to be made of the bending-moment power spectra that could be considered typical for each of the major configurations investigated. (See fig. 8.) The effects of these variations in power spectra fortunately are minimized in the present investigation because the major portion of the model response was in the first bending mode.

CONCLUDING REMARKS

Aerodynamic damping and buffet bending-moment response measurements have been made on a 0.08-scale aeroelastic model of a 2205-inch Saturn I Block II launch vehicle with an Apollo spacecraft payload. In addition to the basic model configuration six other geometrically different configurations were studied. The results are discussed in some detail in the section entitled "Results and Discussion." However, some general comments in the way of summary are in order.

Aerodynamic stiffness effects were found to be small; no discernible change in model frequency was apparent other than the normal scatter in the data between wind-off and wind-on tunnel conditions.

The aerodynamic damping data were positive (stabilizing) for all configurations at an angle of attack of 0° . The aerodynamic damping was generally small in magnitude. Some of the model damping data were scaled to corresponding full-scale values.

The maximum full-scale aerodynamic damping along the trajectory, scaled from model results, was generally less than one-half of the estimated structural and control-system damping. The largest amount measured was about 1.3 percent of critical damping.

Some comparisons of experimental and calculated aerodynamic damping data were made. Calculated values of aerodynamic damping which account for separated-flow effects agreed well with the measured values of damping for the Apollo configurations with and without a flow separator except for the third mode. Agreement of aerodynamic damping derivatives calculated from momentum theory on the body and from a quasi-steady approach (using measured static normal force derivatives) on the fins with measured values was erratic.

The variation of model root-mean-square bending moment with Mach number was similar for all configurations studied; the maximum value occurred at a Mach number of about 0.9. Model bending-moment response increased with increasing angle of attack. Some of the model data were scaled to corresponding full-scale values. However, no actual flight data were available for comparison.

end

Langley Research Center,
National Aeronautics and Space Administration,
Langley Station, Hampton, Va., December 3, 1964.

REFERENCES

1. Hanson, Perry W.; and Doggett, Robert V., Jr.: Wind-Tunnel Measurements of Aerodynamic Damping Derivatives of a Launch Vehicle Vibrating in Free-Free Bending Modes at Mach Numbers From 0.70 to 2.87 and Comparisons With Theory. NASA TN D-1391, 1962.
2. Hanson, Perry W.; and Doggett, Robert V., Jr.: Aerodynamic Damping of a 0.02-Scale Saturn SA-1 Model Vibrating in the First Free-Free Bending Mode. NASA TN D-1956, 1963.
3. Doggett, Robert V., Jr.; and Hanson, Perry W.: An Aeroelastic Model Approach for the Prediction of Buffet Bending Loads on Launch Vehicles. NASA TN D-2022, 1963.
4. Ericson, Lars-Eric; and Reding, J. Peter: Report on Saturn I-Apollo Unsteady Aerodynamics. LMSC-A650215 (Contract NAS 8-5338), Lockheed Missiles & Space Co., Feb. 1964.
5. Garrick, I. E.: Some Research on High-Speed Flutter. Third Anglo-American Aero. Conf., Sept. 4-7, 1951 (Brighton, England). R.A.S., 1952, pp. 419-446J.
6. Bisplinghoff, Raymond L.; Ashley, Holt; and Halfman, Robert L.: Aeroelasticity. Addison-Wesley Pub. Co., Inc. (Cambridge, Mass.), c.1955.
7. Mazet, R.: Some Aspects of Ground and Flight Vibration Tests. AGARD Rept. 40-T, Apr. 1956.
8. Olsson, Carl Olof; and Orlik-Rückemann, Kazimierz: An Electronic Apparatus for Automatic Recording of the Logarithmic Decrement and Frequency of Oscillations in the Audio and Subaudio Frequency Range. Rep. No. 52, Aero. Res. Inst. of Sweden (Stockholm), 1954.
9. Rice, S. O.: Mathematical Analysis of Random Noise. Bell System Tech. J. Pts. I and II, vol. XXIII, no. 3, July 1944, pp. 282-332. Pts. III and IV, vol. XXIV, no. 1, Jan. 1945, pp. 46-156.
10. Liepmann, H. W.: On the Application of Statistical Concepts to the Buffeting Problem. J. Aeron. Sci., vol. 19, no. 12, Dec. 1952, pp. 793-800, 822.
11. Ernsberger, Gale R.: Dynamic Test Results of SAD-6. NASA TM X-53029, April 1964.

TABLE 1

MODEL PHYSICAL PROPERTIES

Physical property	Model configuration						
	Basic Apollo configuration			Basic Apollo configuration without escape system		Jupiter configuration	
	Basic Apollo configuration with flow separator			Basic Apollo configuration without fins		Jupiter configuration with modified fins	
	Basic Apollo configuration without fins					Jupiter configuration without fins	
	Free-free bending modes						
	First	Second	Third	First	Second	First	Second
f, cps	11.04	18.27	30.42	13.38	26.85	13.87	28.65
M _s , slugs	0.158	0.087	0.128	0.868	0.479	0.561	0.236
C _{cr} , lb-sec/ft	21.9	20.0	49.0	145.8	161.3	97.6	84.9
$\int_0^{L/r} \left[\frac{R(\frac{x}{L})}{r} \right]^2 \left(\frac{x}{L} \right) d\left(\frac{x}{L} \right)$	0.261	0.231	0.292	1.288	0.695	0.870	0.428
C _s /C _{cr}	0.00092	0.0034	0.0027	0.0028	0.0078	0.0028	0.0140
f _g , cps	1.70			1.85		1.88	
W, lb	784			781		777	
x _{cg} , in.	46.6			----		45.4	
Values of C _g /C _{cr} for rigid-body pitch mode of basic Apollo configuration (results from model suspension system) . . 0.05 to 0.07							
Basic-fin (large) frequencies:							
Bending						275 cps	
Torsion						370 cps	

TABLE 2

FULL-SCALE VEHICLE TRAJECTORY AND PHYSICAL PROPERTIES USED IN MODEL DESIGN AND DATA REDUCTION

Time from lift-off, sec	M	q, lb/ft ²	ρV, lb-sec/ft ³	W, lb	Free-free bending modes								
					First			Second			Third		
					f ₁ , cps	M _S , slugs	C _c /C _{cr}	f ₂ , cps	M _S , slugs	C _c /C _{cr}	f ₃ , cps	M _S , slugs	C _c /C _{cr}
Saturn-Apollo with and without flow separator													
46	0.80	510	1.187	8.37 × 10 ⁵	1.81	168.1	0.0500	3.00	92.8	0.0024	4.97	136.5	0.0028
50	.90	570	1.196	8.17	1.84	164.2	.0467	3.04	90.6	.0024	5.02	133.3	.0027
52	1.00	615	1.172	8.00	1.85	161.0	.0450	3.07	88.8	.0023	5.07	130.7	.0027
56	1.11	645	1.130	7.83	1.87	157.5	.0415	3.11	86.9	.0022	5.13	127.9	.0026
59	1.18	655	1.092	7.66	1.89	154.0	.0390	3.14	85.0	.0021	5.19	125.0	.0025
Saturn-Apollo without escape system													
46	0.80	510	1.187	8.32 × 10 ⁵	2.22	931.0	0.0194	4.39	514.0	0.0011			
50	.90	570	1.196	8.12	2.25	909.0	.0186	4.42	500.5	.0009			
52	1.00	615	1.172	7.95	2.27	890.0	.0184	4.49	491.0	.0009			
56	1.11	645	1.130	7.78	2.30	871.0	.0193	4.54	480.0	.0013			
58	1.15	653	1.106	7.58	2.33	848.0	.0207	4.60	468.0	.0017			
Jupiter nose with and without fins													
46	0.80	510	1.187	8.30 × 10 ⁵	2.23	629.0	0.0194	4.57	278.8	0.0011			
50	.90	570	1.196	8.10	2.29	596.0	.0186	4.62	258.3	.0009			
52	1.00	615	1.172	7.91	2.34	571.0	.0184	4.79	240.3	.0009			
56	1.11	645	1.130	7.72	2.40	543.0	.0193	4.92	224.5	.0013			
59	1.19	655	1.092	7.50	2.47	512.0	.0207	5.05	216.3	.0017			
Note: Full-scale structural damping ratio assumed to be 0.014 and 0.022 for the first and second flexible modes, respectively, of the Jupiter configuration and the Saturn-Apollo configuration without escape system. Values of structural damping in the first, second, and third flexible modes of the basic Apollo configuration are 0.011, 0.012, and 0.010, respectively.													

Note: Full-scale structural damping ratio assumed to be 0.014 and 0.022 for the first and second flexible modes, respectively, of the Jupiter configuration and the Saturn-Apollo configuration without escape system. Values of structural damping in the first, second, and third flexible modes of the basic Apollo configuration are 0.011, 0.012, and 0.010, respectively.

^aDesign point.

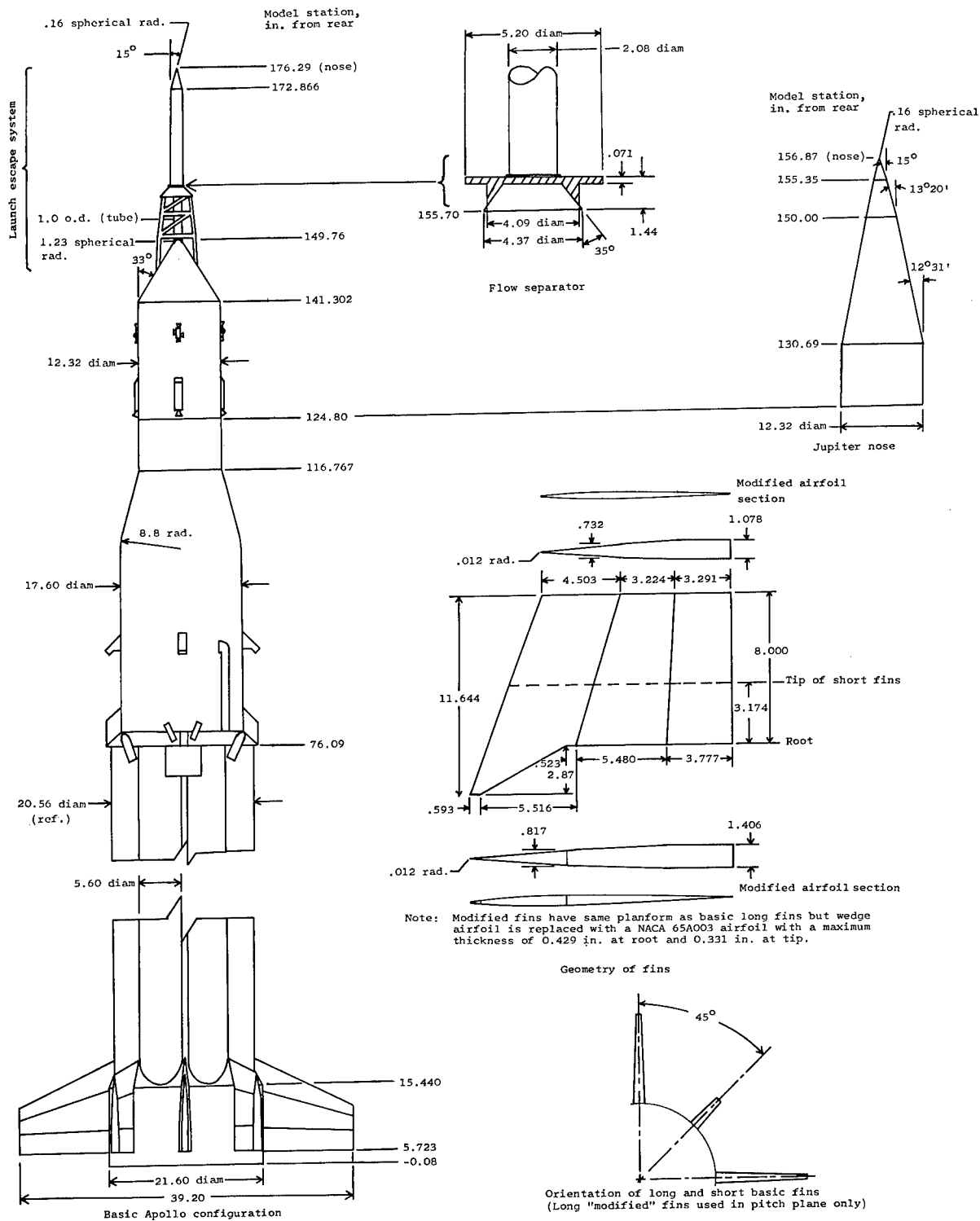


Figure 1.- Geometry of model and components. (All dimensions in inches unless noted otherwise.)

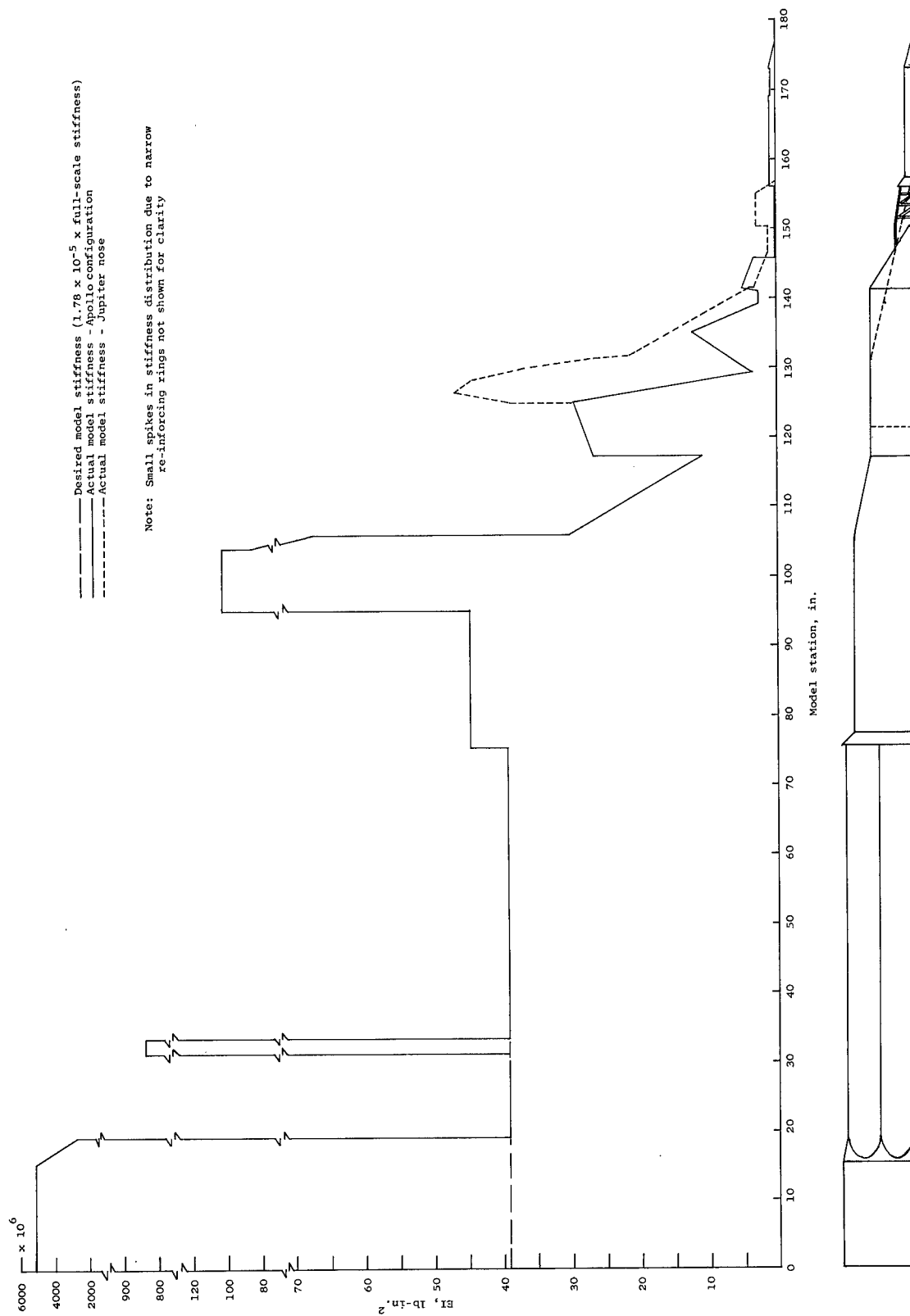


Figure 2.- Bending stiffness distributions.

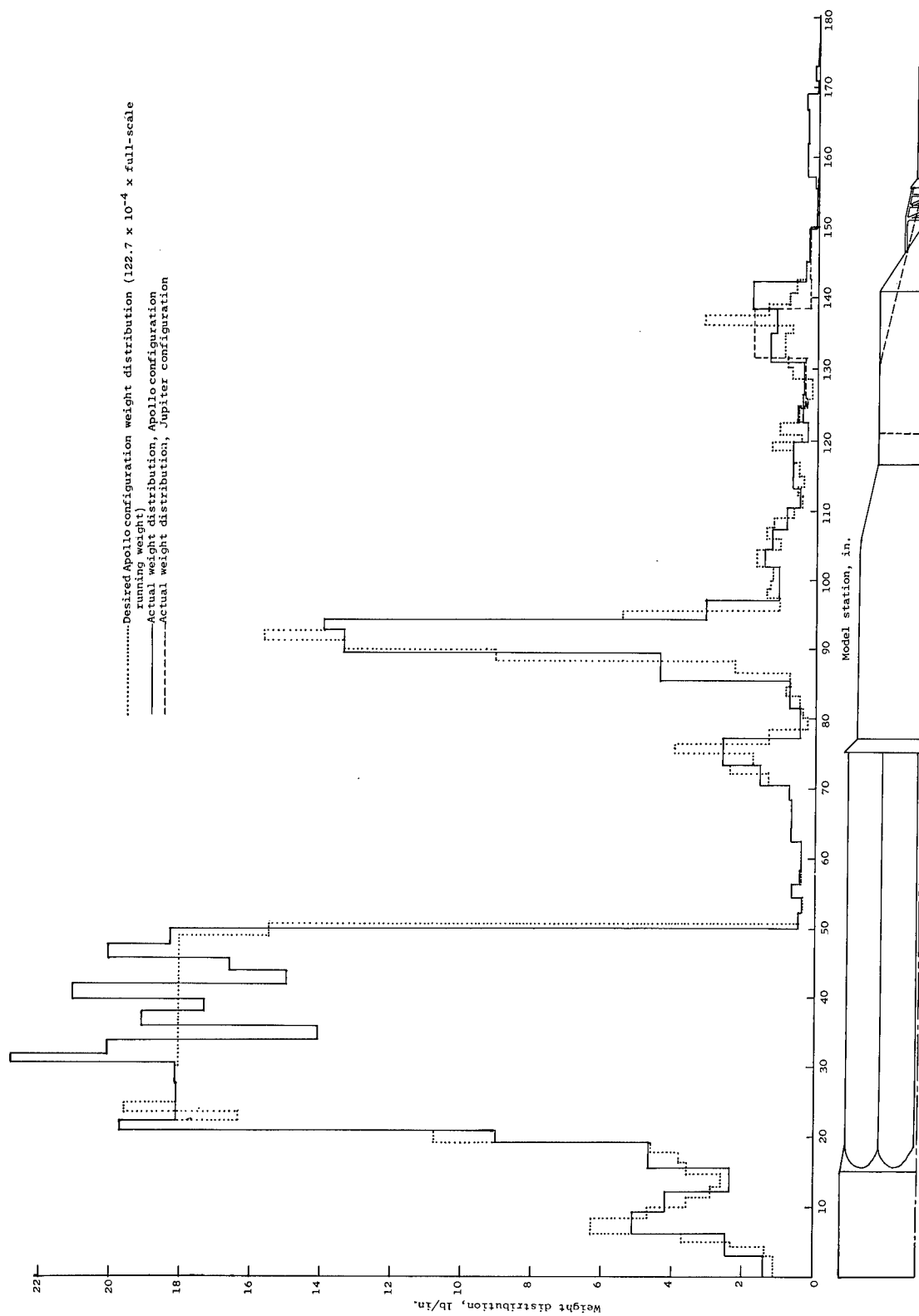
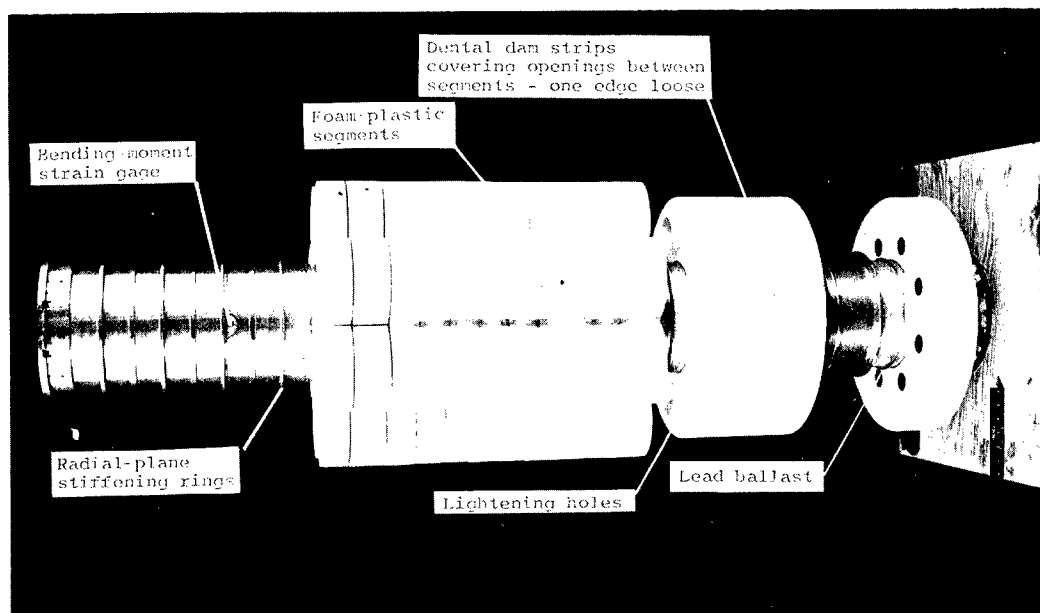
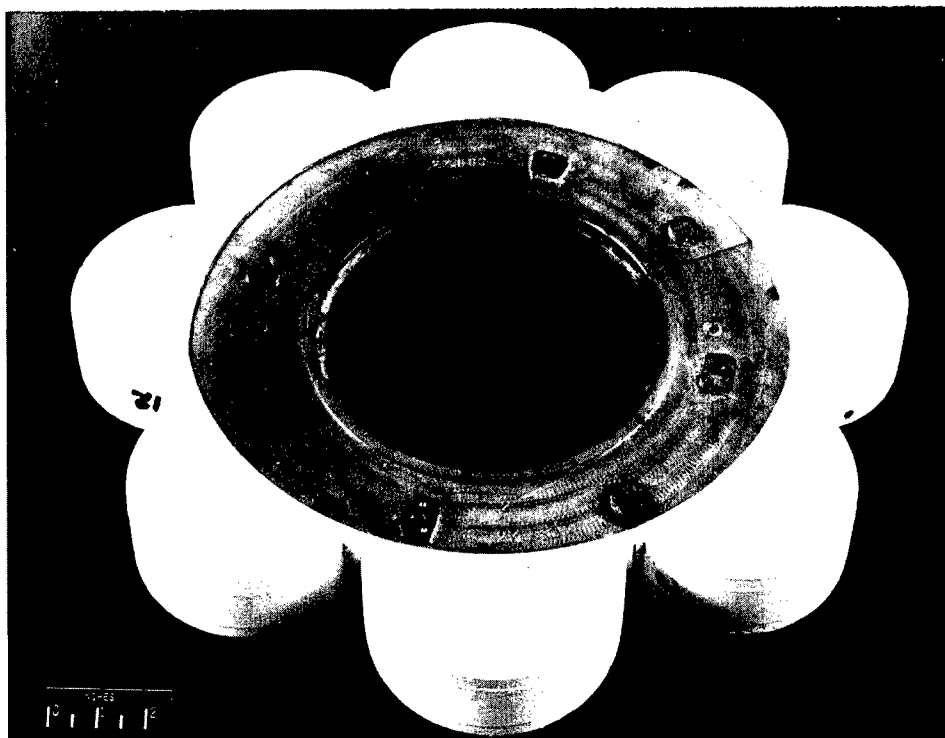


Figure 3.- Weight distributions.



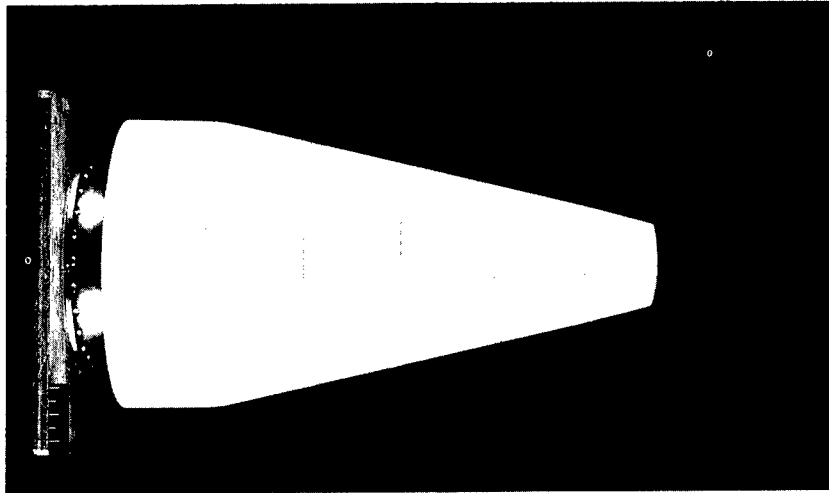
(a) Central structural tube with some segments attached.



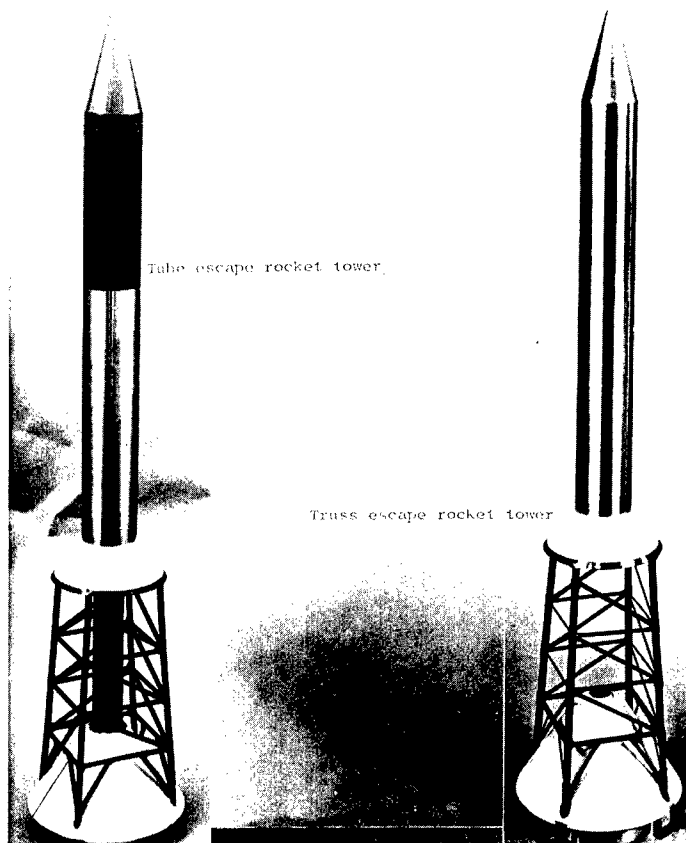
(b) Typical ballasted foam-plastic segment.

L-64-10220

Figure 4.- Photographs of model and components showing construction details.



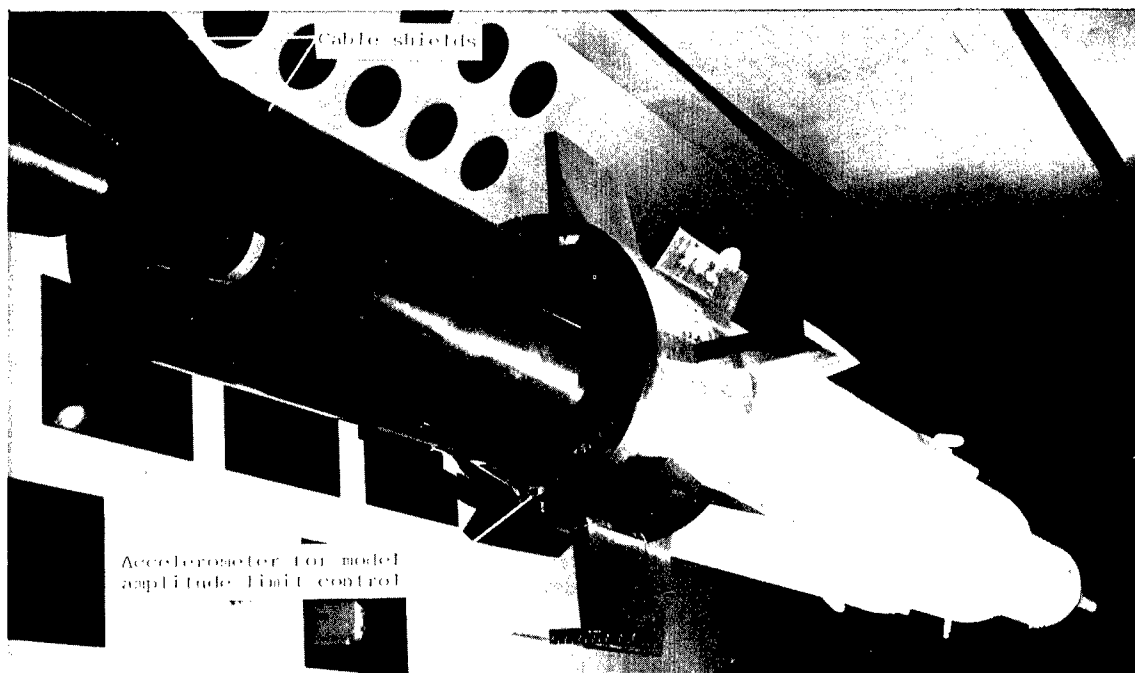
(c) Segmented Jupiter nose cone.



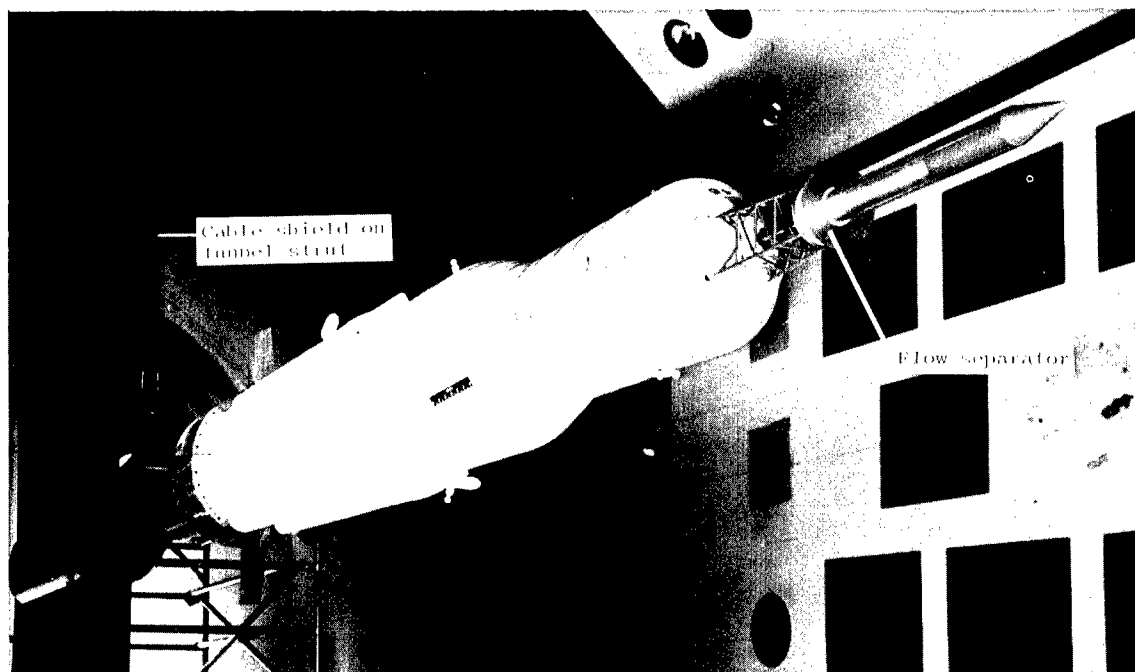
(d) Escape rocket assemblies.

Figure 4.- Continued.

L-64-10221



(e) Model mounted in Langley transonic dynamics tunnel; lower rear view.



(f) Model mounted in Langley transonic dynamics tunnel; lower front view.

Figure 4.- Concluded.

L-64-10222

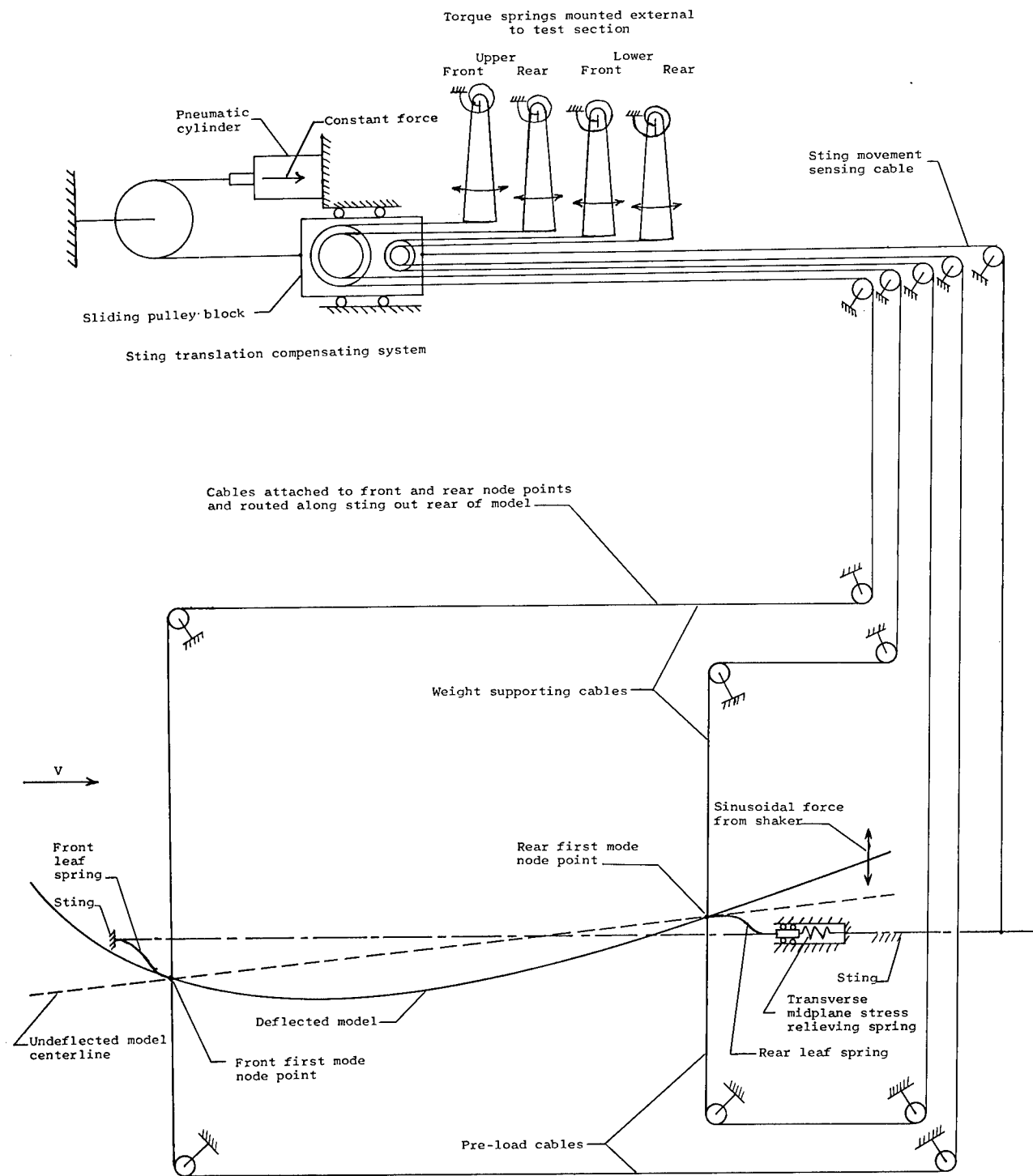
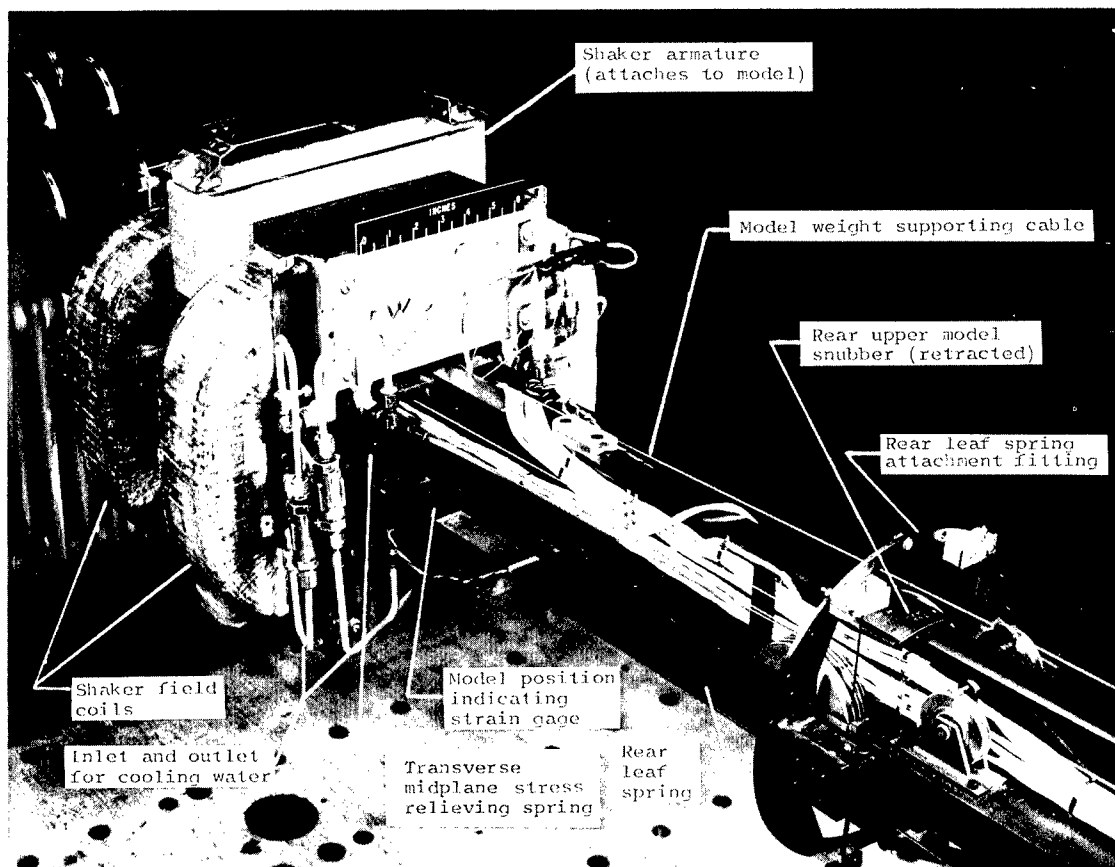
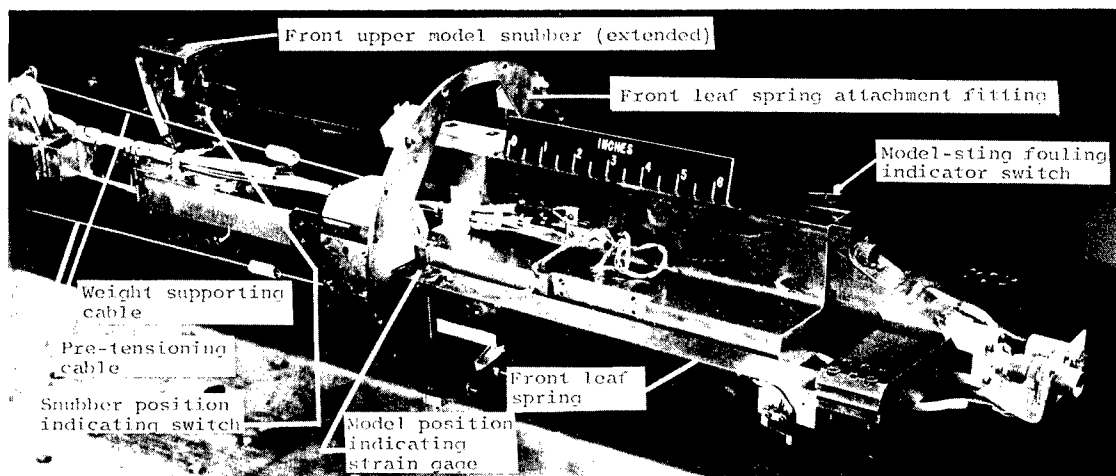


Figure 5.- Model support system.



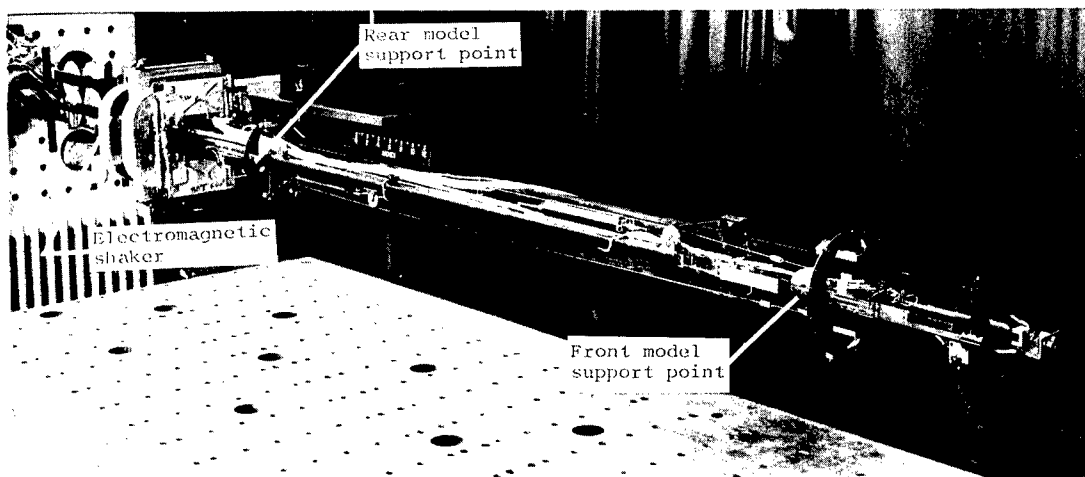
(b) Rear portion of sting.



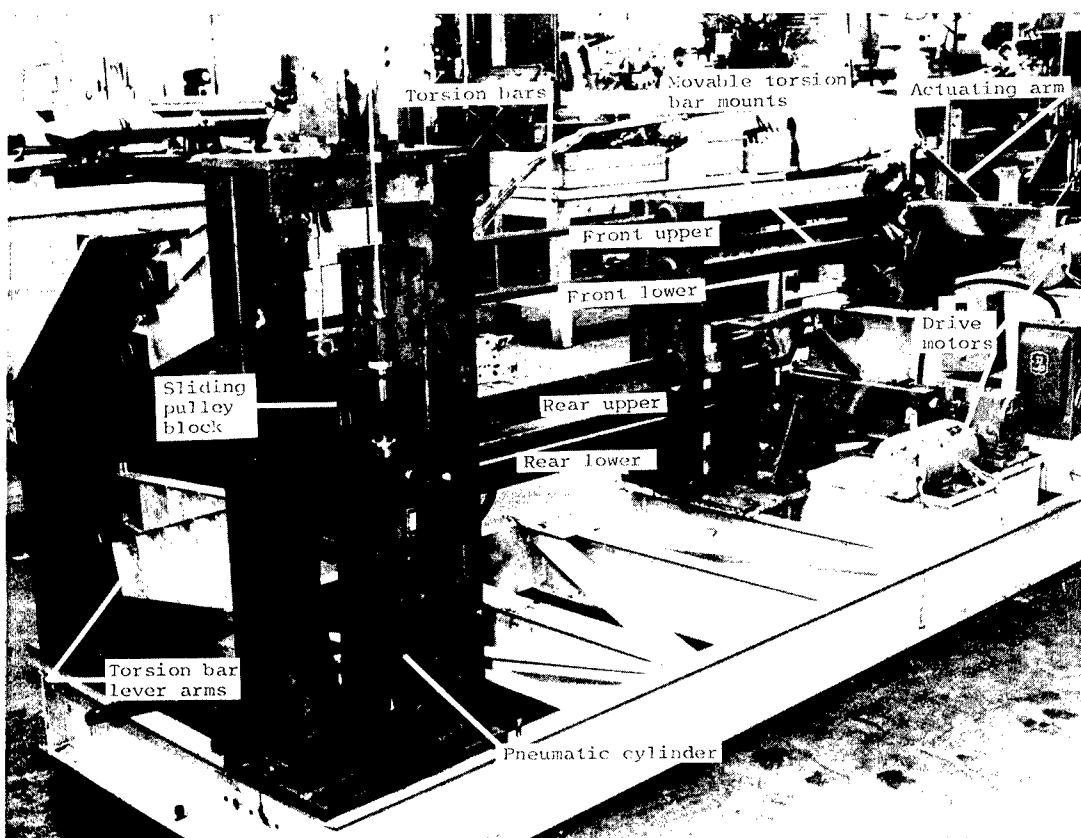
(c) Front portion of sting.

Figure 5.- Continued.

L-64-10223

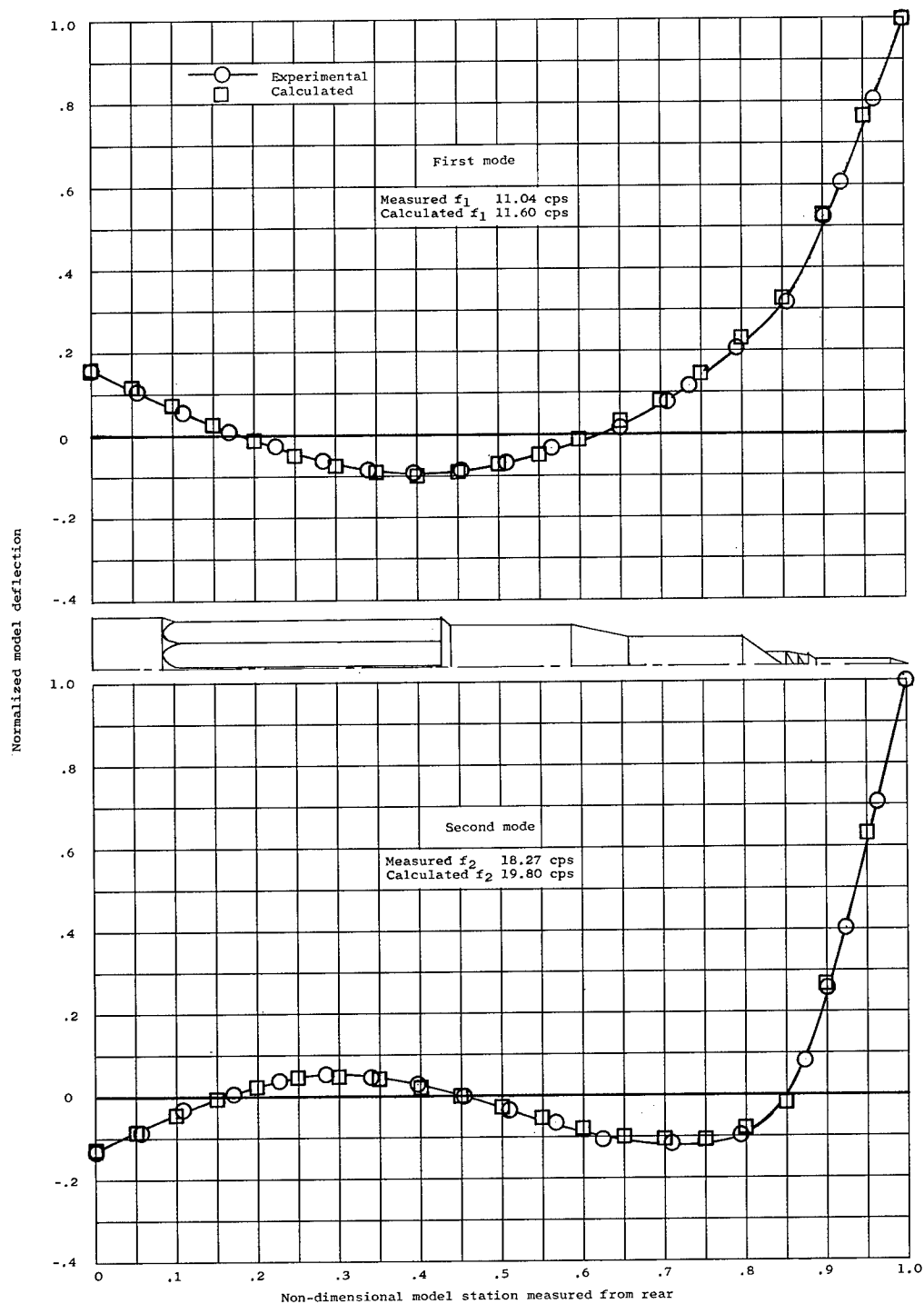


(d) Overall view of sting.



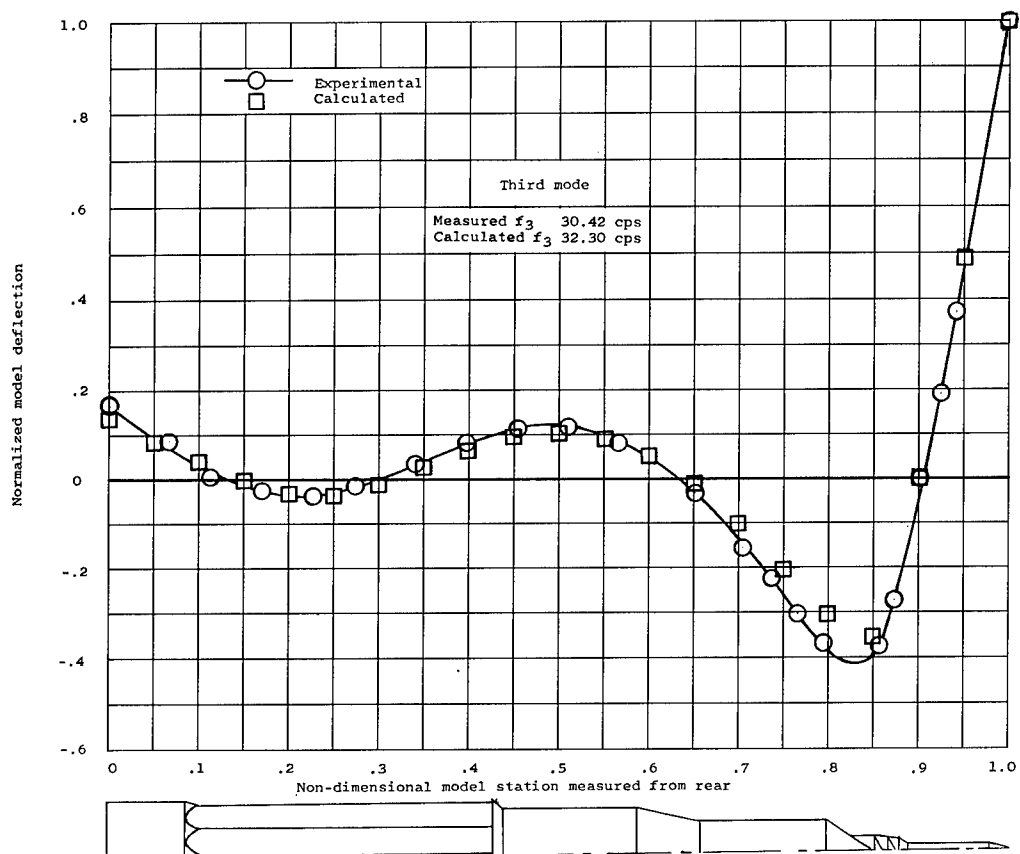
(e) Portion of support system external to test section.

Figure 5.- Concluded. L-64-10224



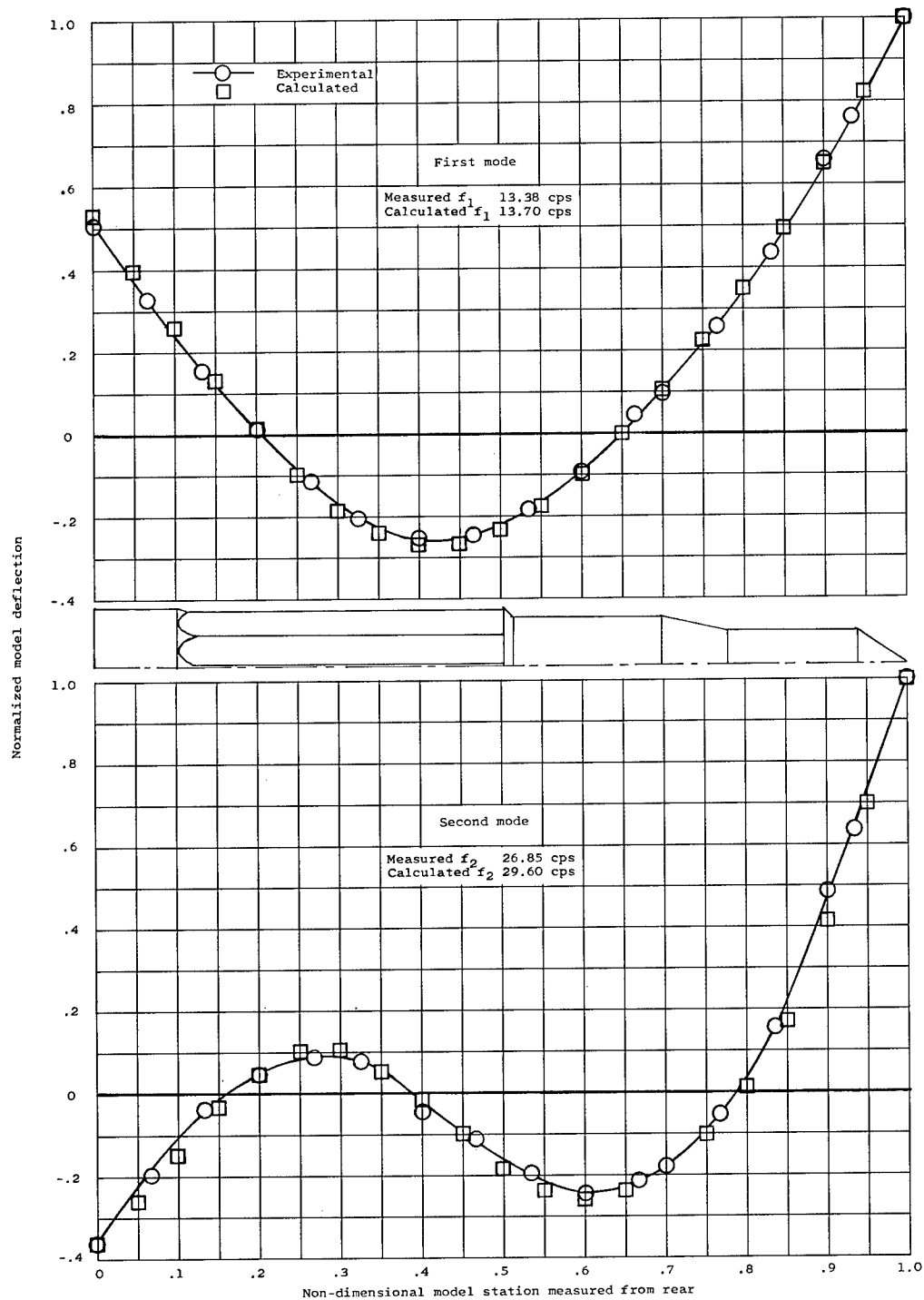
(a) Apollo configuration with and without flow separator on escape rocket; first and second modes.

Figure 6.- Calculated and measured free-free bending mode shapes.



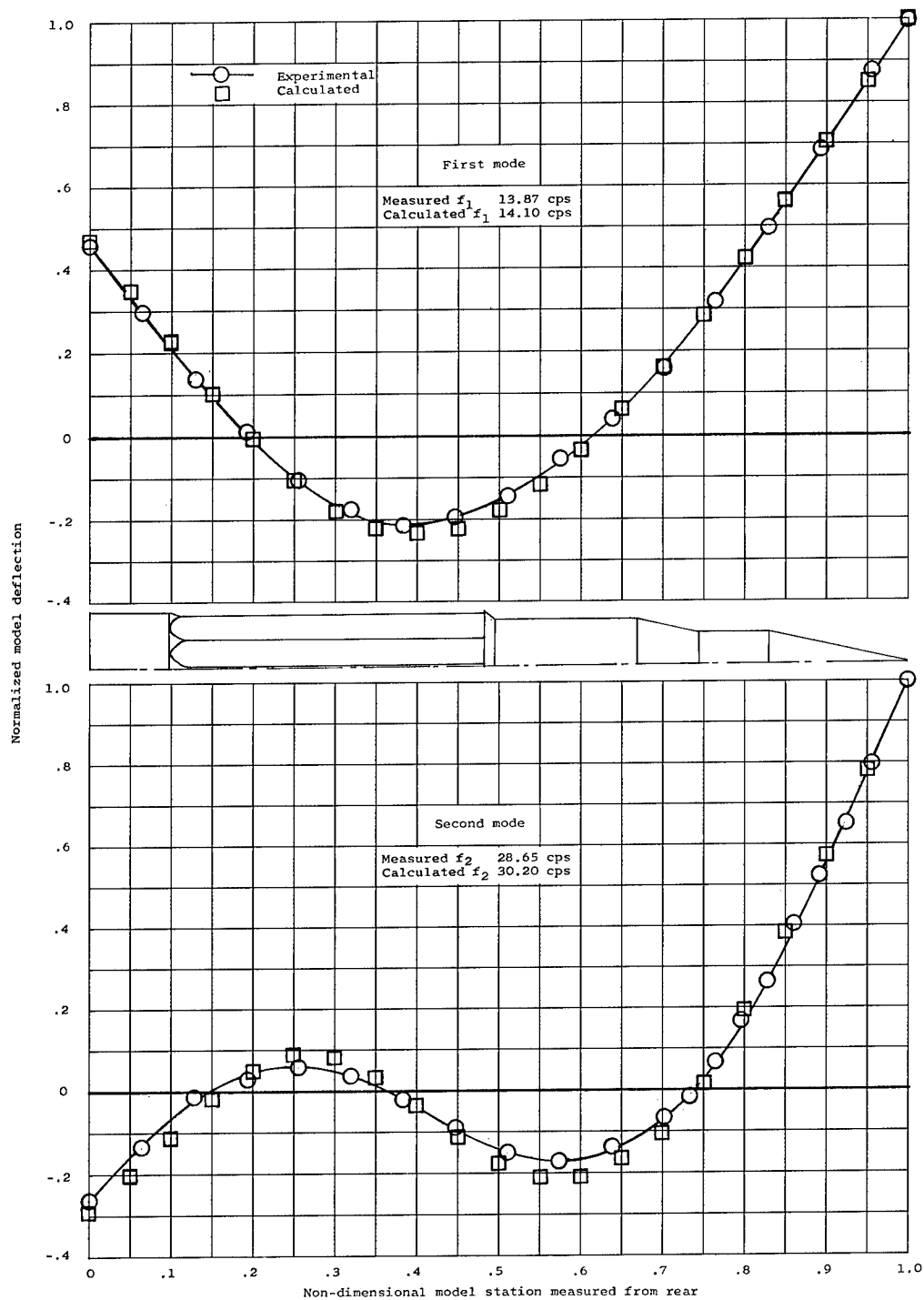
(b) Apollo configuration with and without flow separator on escape rocket; third mode.

Figure 6.- Continued.



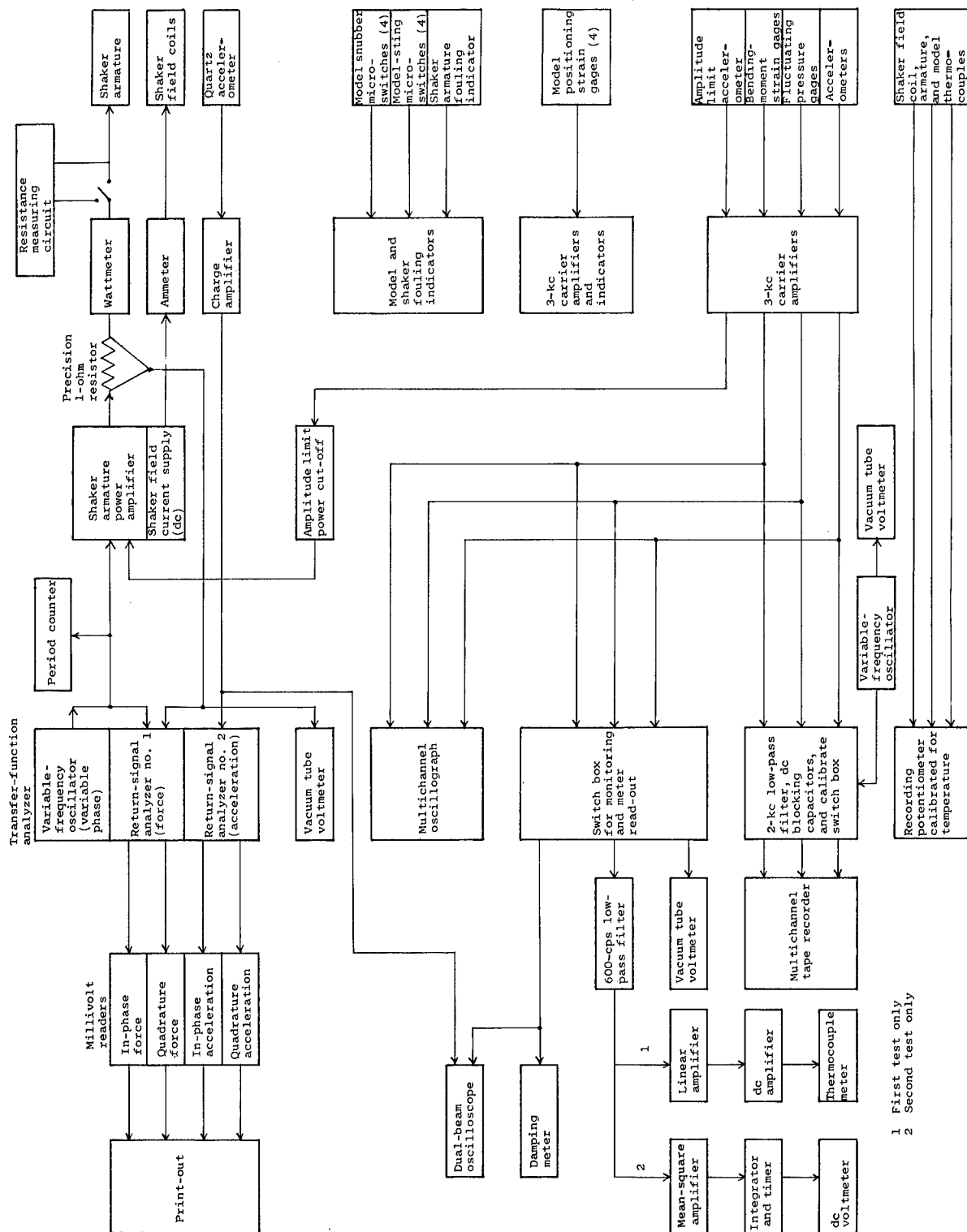
(c) Apollo configuration without escape tower and rocket; first and second modes.

Figure 6.- Continued.



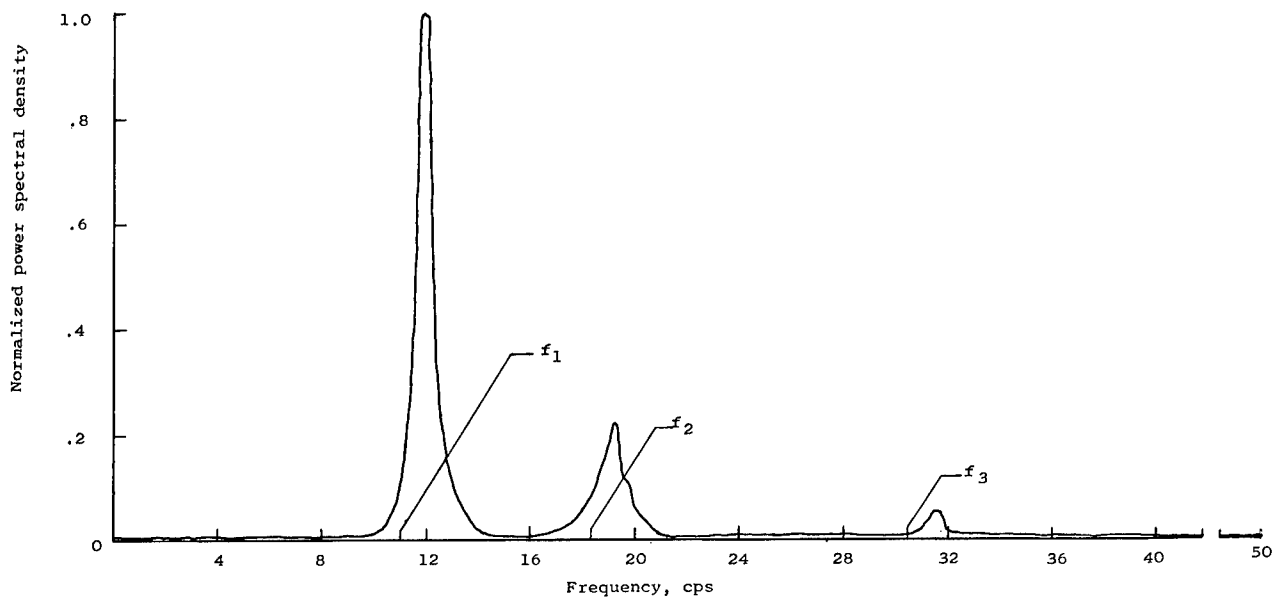
(d) Jupiter nose cone configuration with and without fins; first and second modes.

Figure 6.- Concluded.

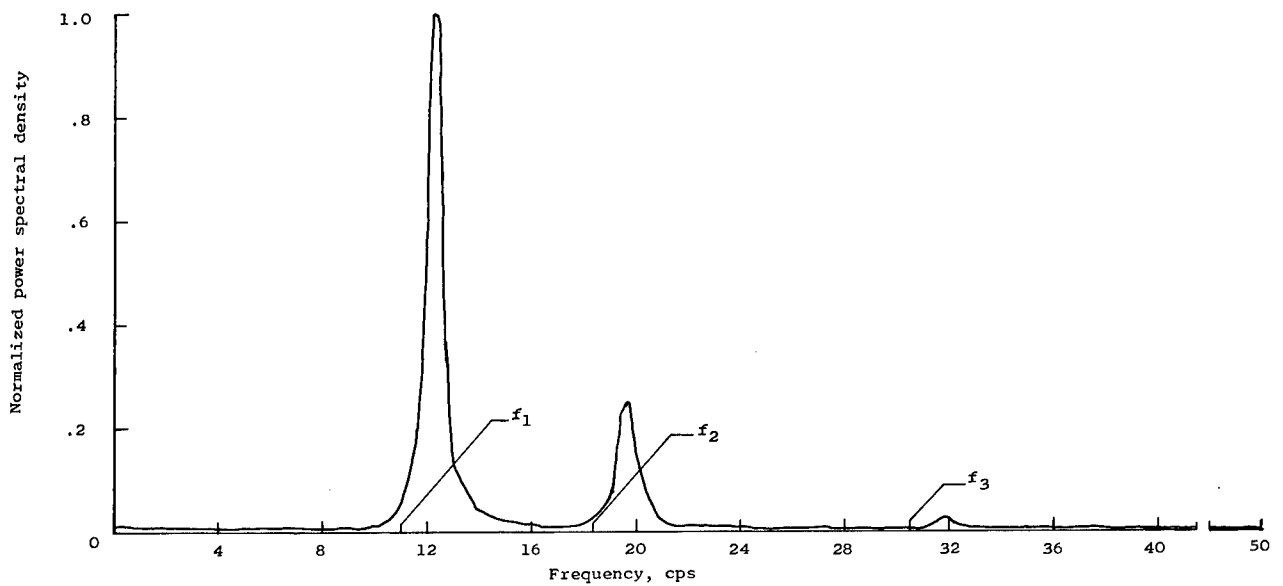


1 First test only
2 Second test only

Figure 7.- Block diagram of model, shaker, and read-out instrumentation.

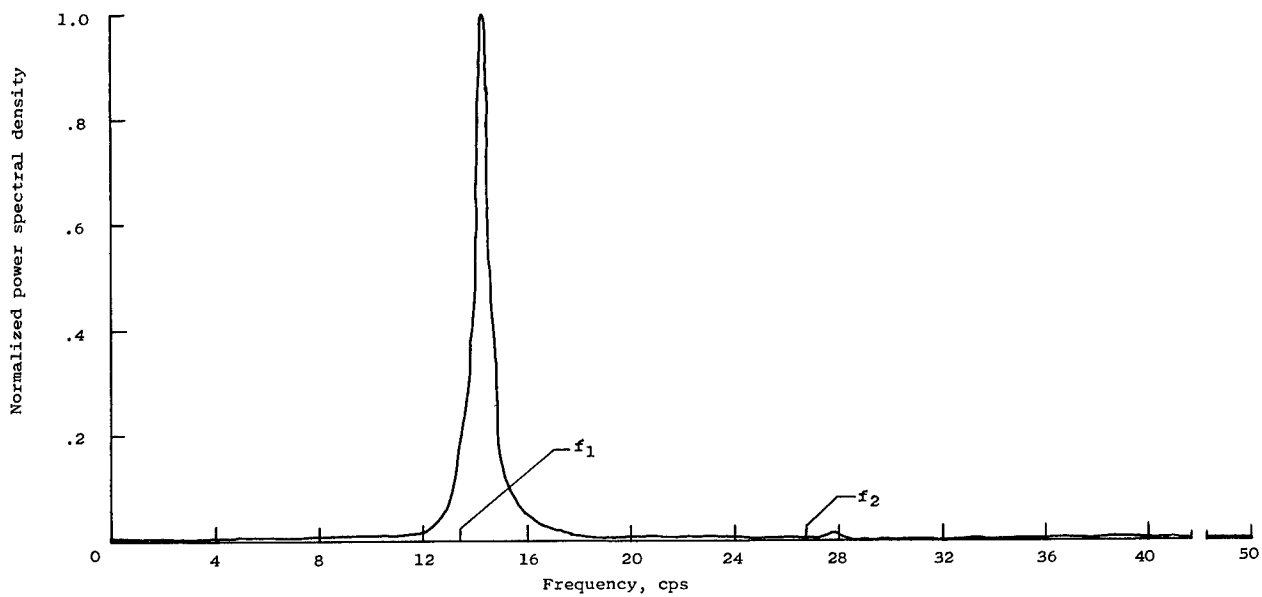


(a) Apollo configuration without flow separator on escape rocket.

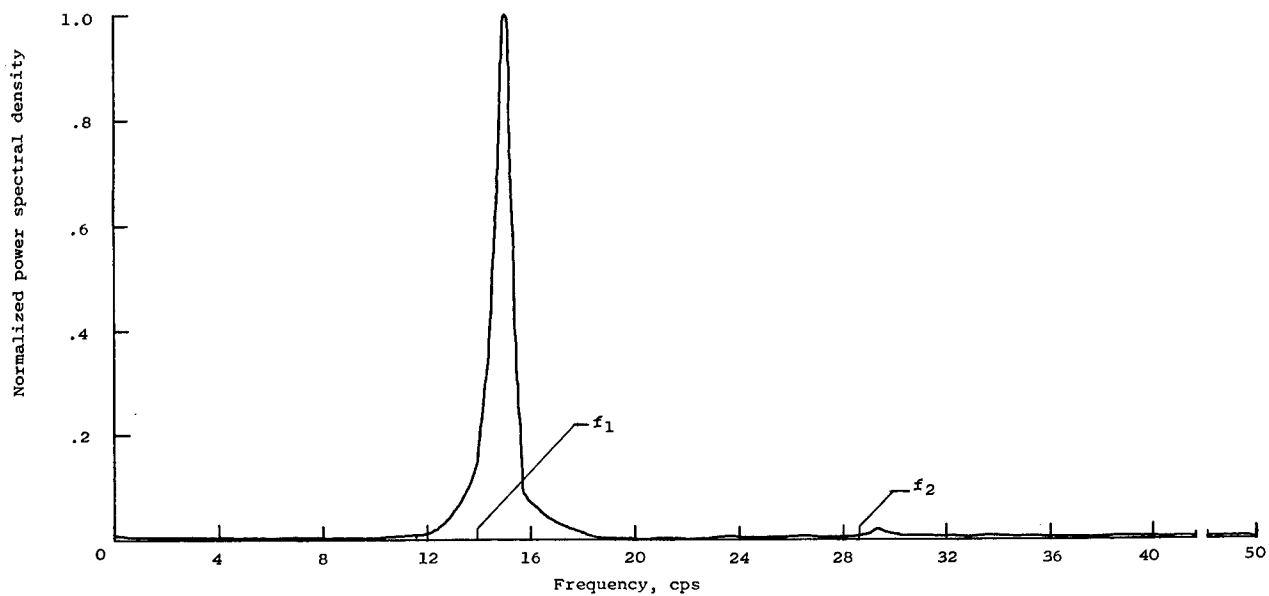


(b) Apollo configuration with flow separator on escape rocket.

Figure 8.- Sample bending-moment power spectral densities. $M = 0.9$; $\alpha = 0^\circ$.



(c) Apollo configuration without escape tower and rocket.



(d) Jupiter nose cone configuration.

Figure 8.- Concluded.

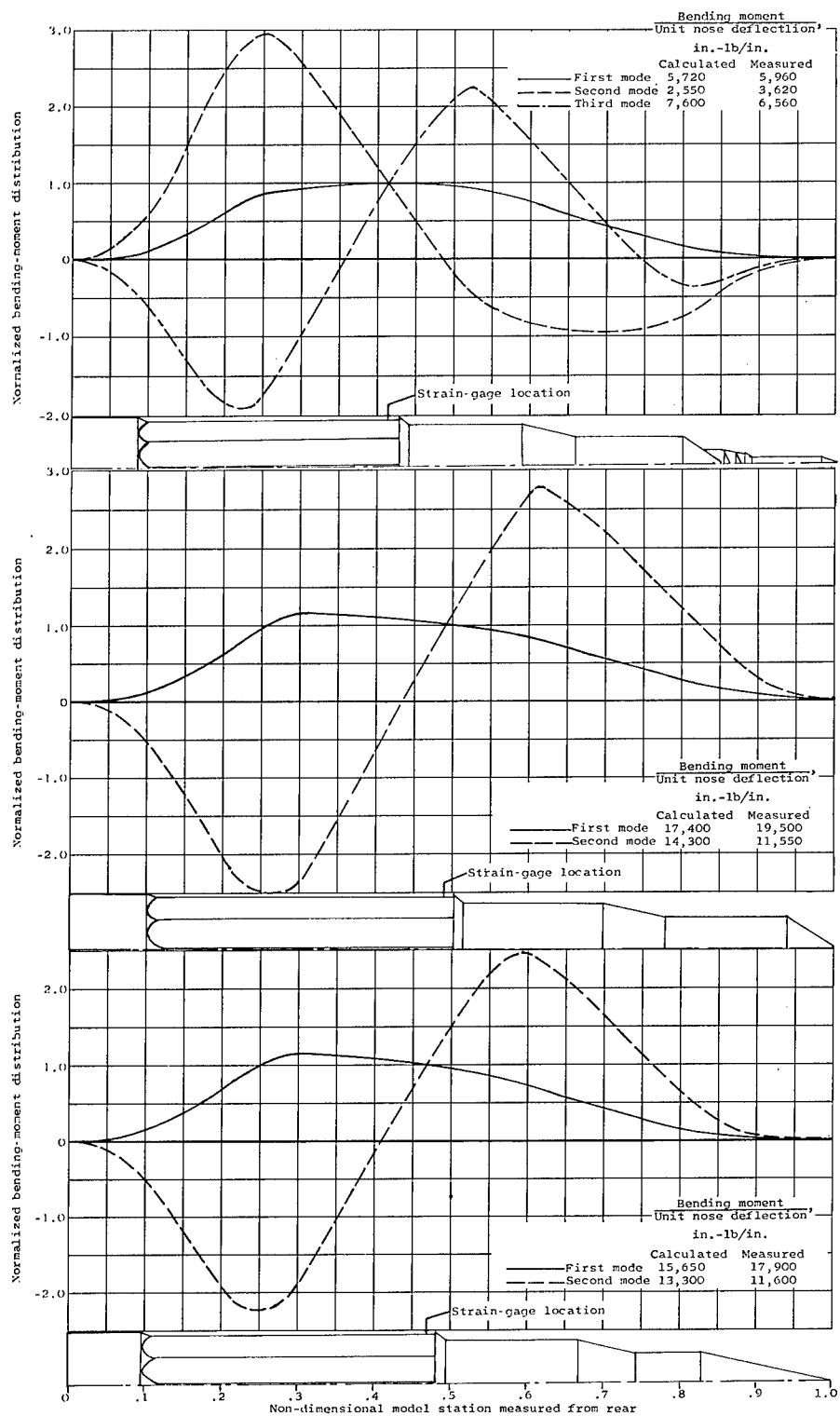
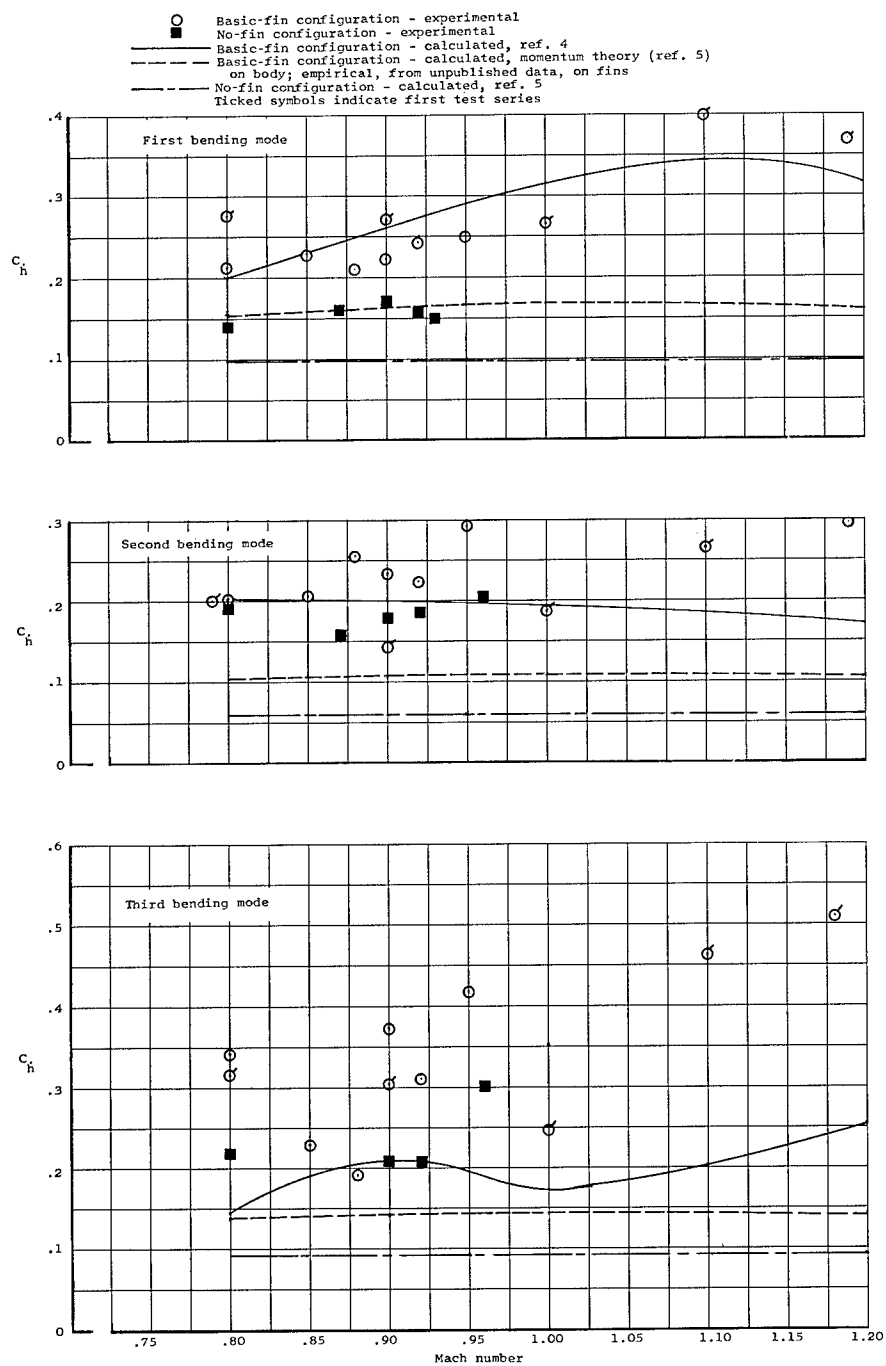


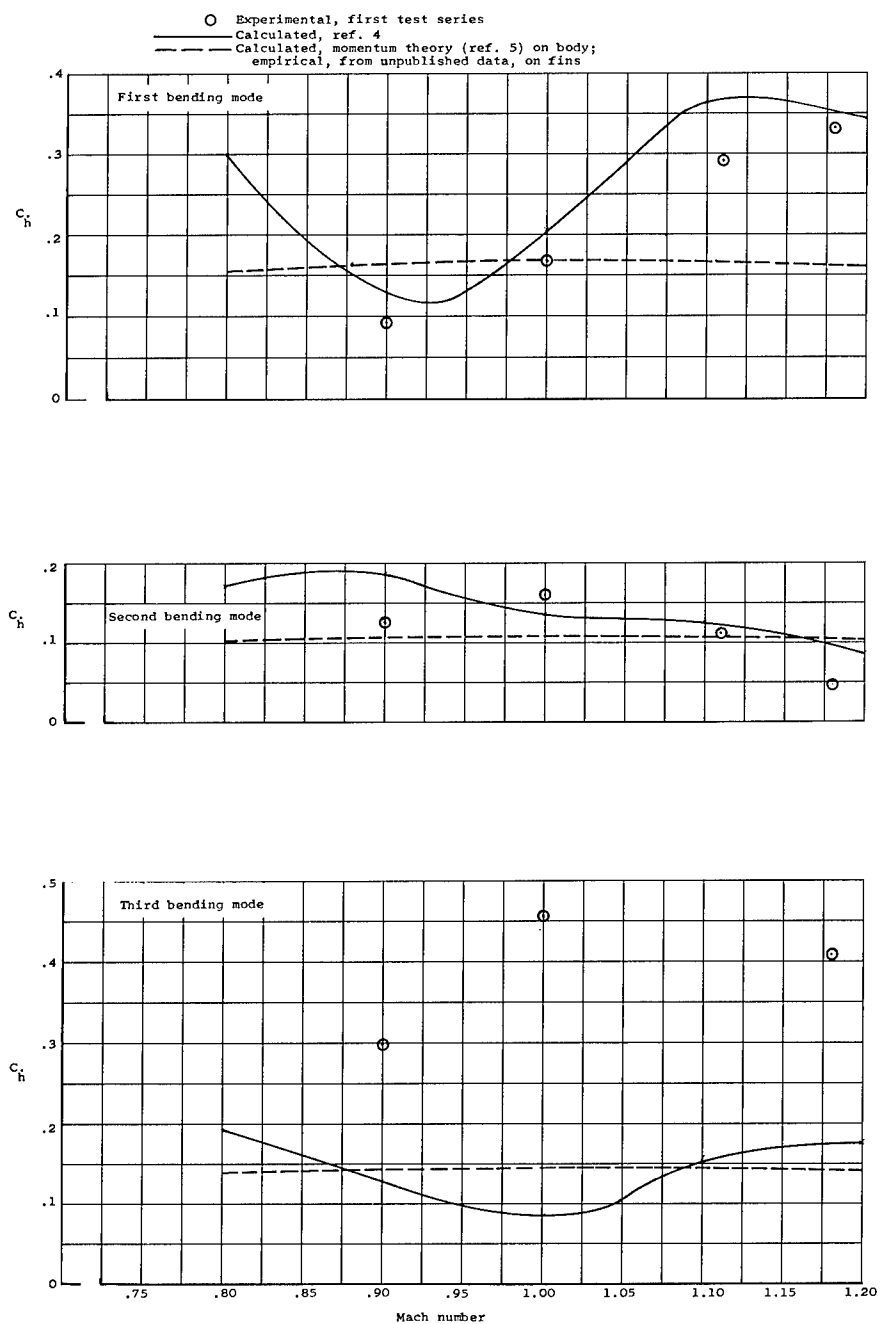
Figure 9.- Bending-moment strain-gage-location sensitivity factors.



(a) Apollo configuration without flow separator; with basic fins and without fins.

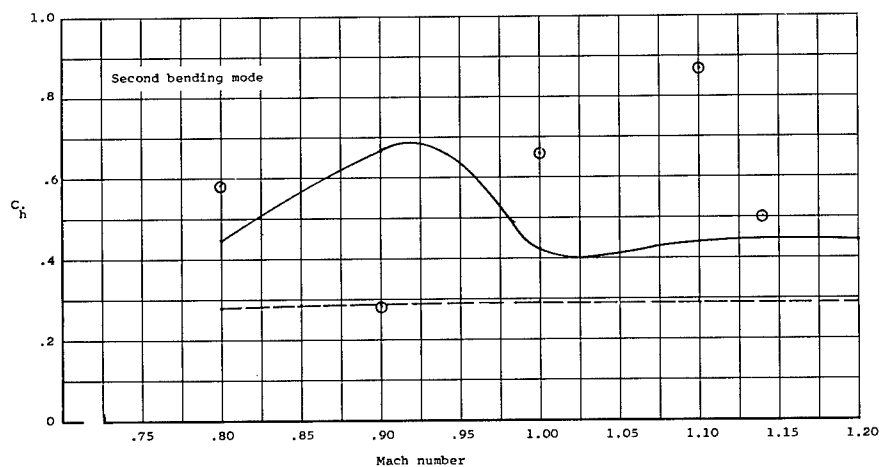
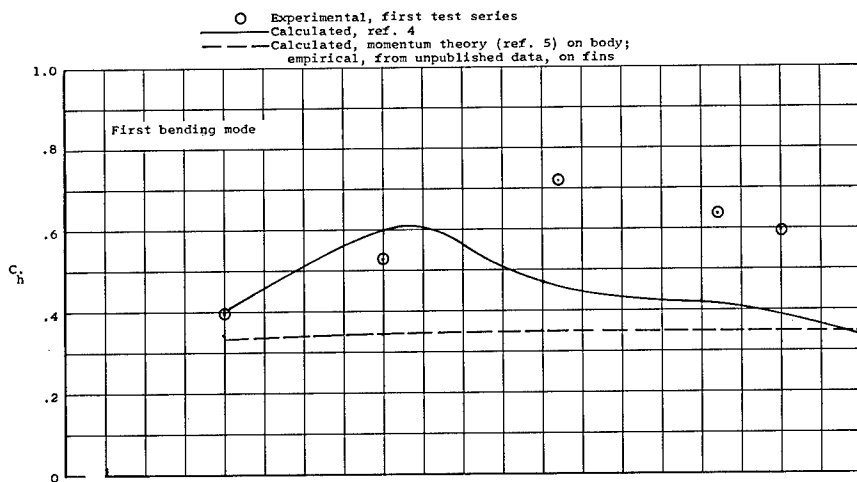
Figure 10.- Variation of aerodynamic damping derivative with Mach number.

$$C_h = 2 \mu k \frac{C_a}{C_{cr}}$$



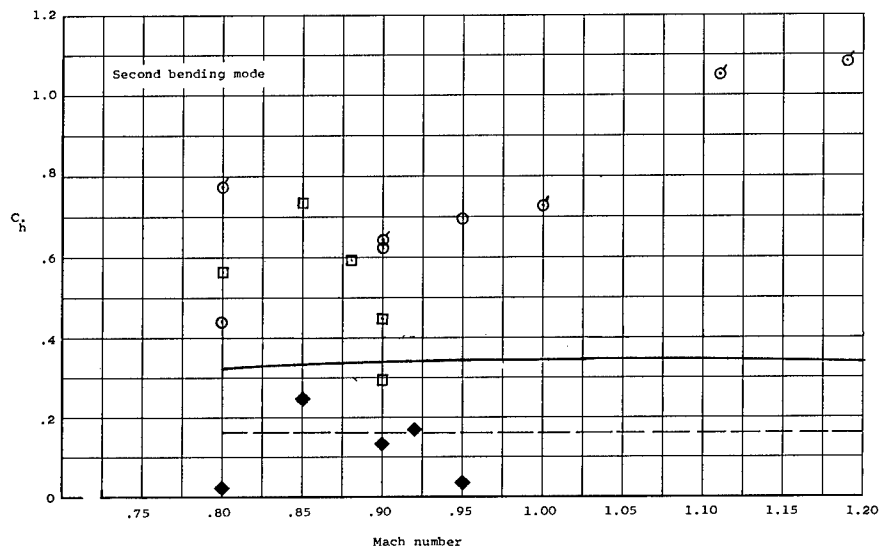
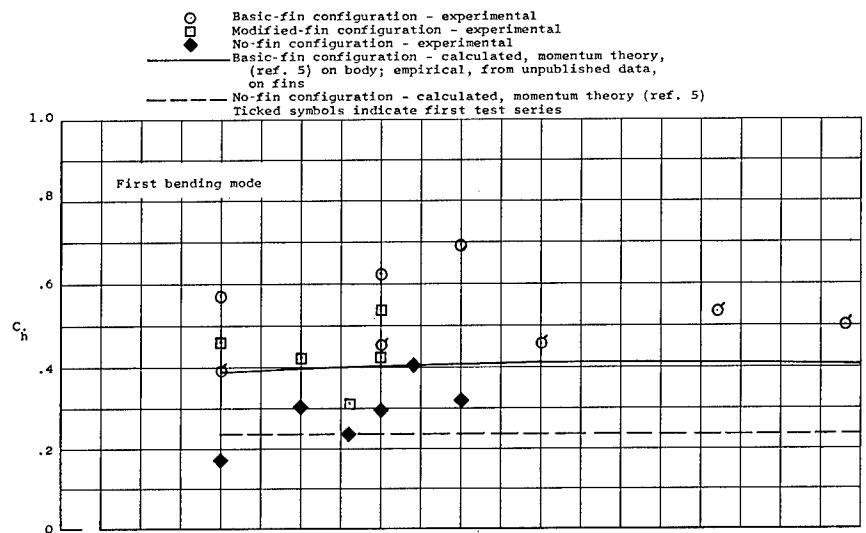
(b) Apollo configuration with flow separator and basic fins.

Figure 10.- Continued.



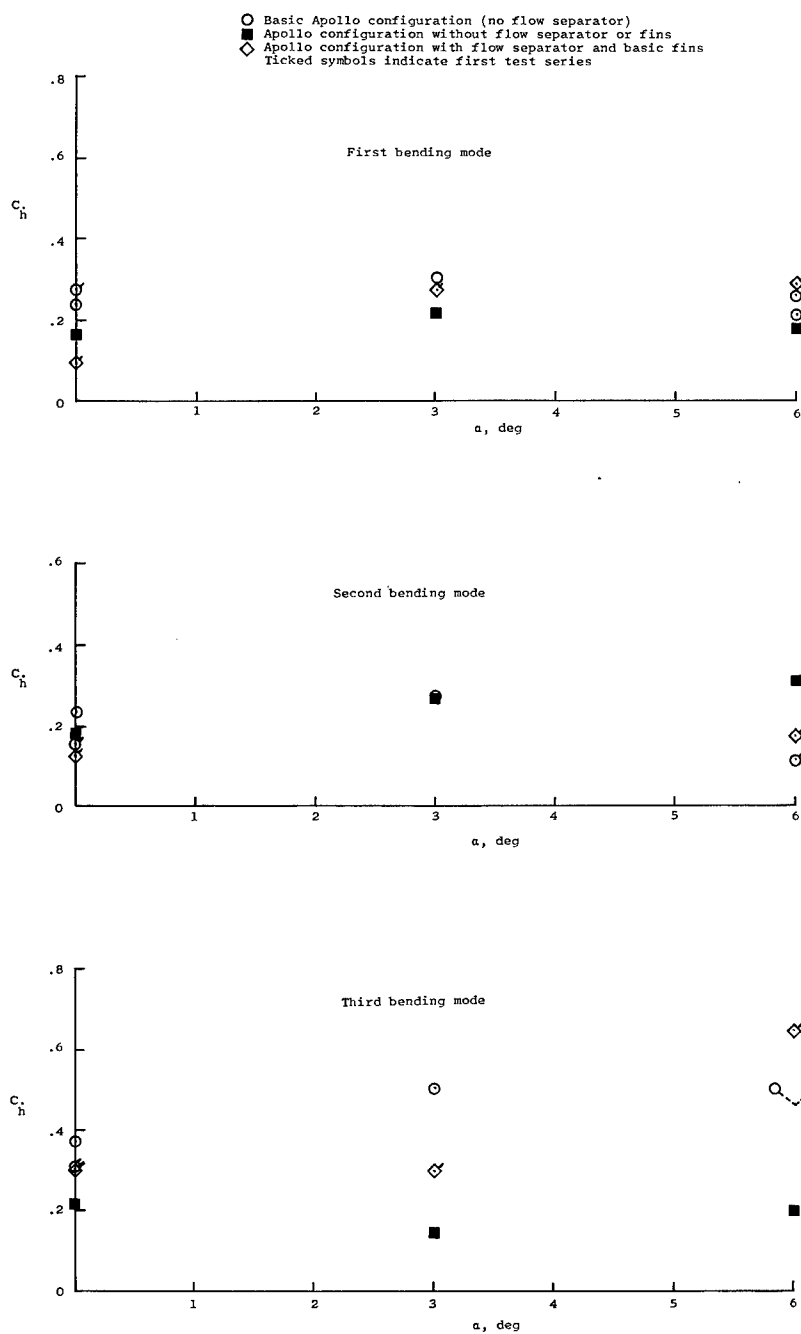
(c) Apollo configuration with basic fins but without escape system.

Figure 10.- Continued.



(d) Jupiter configuration with basic fins, with modified fins, and without fins.

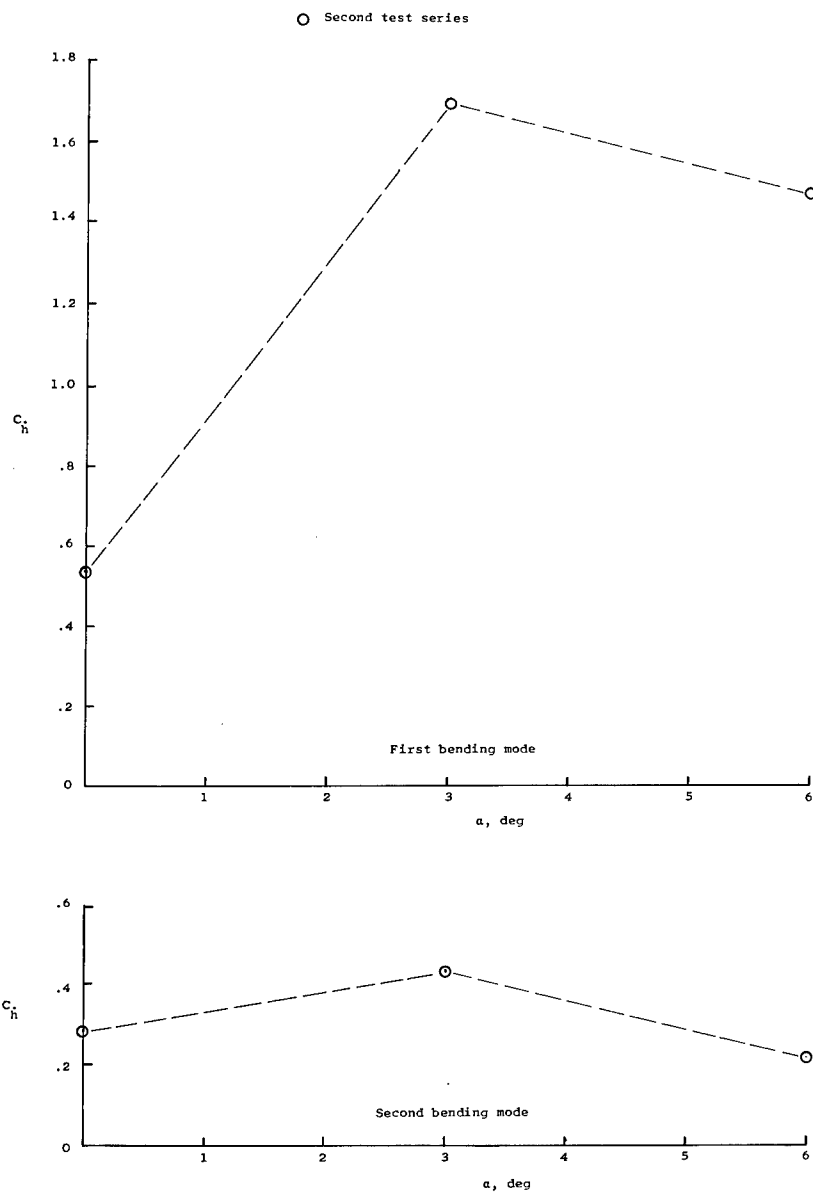
Figure 10.- Concluded.



(a) Apollo configurations with escape system.

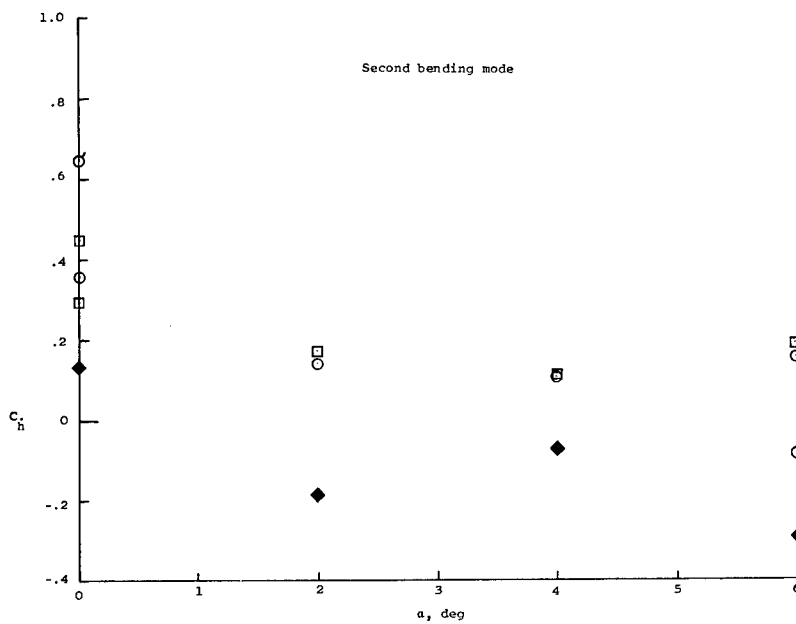
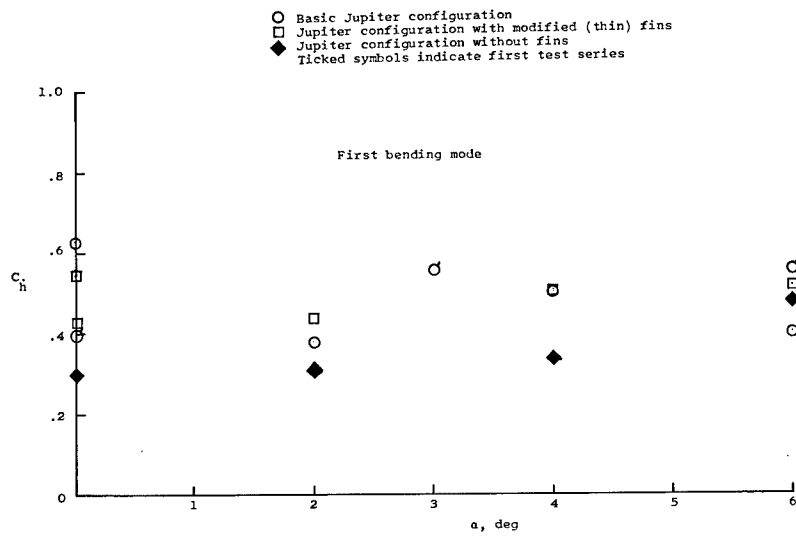
Figure 11.- Variations of aerodynamic damping derivative with angle of attack at $M = 0.9$.

$$C_h = 2\mu k \frac{C_a}{C_{cr}}$$



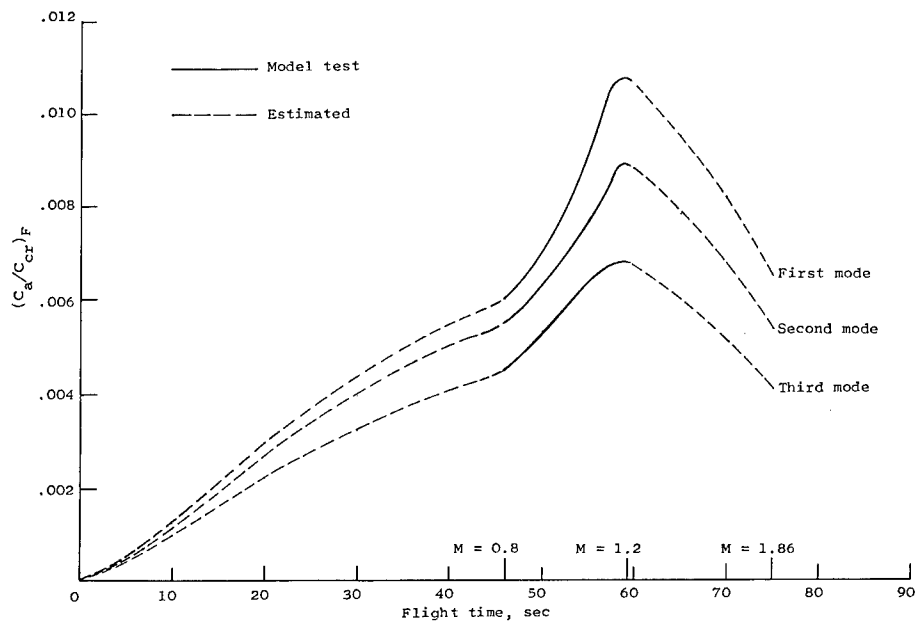
(b) Apollo configuration without escape system.

Figure 11.- Continued.

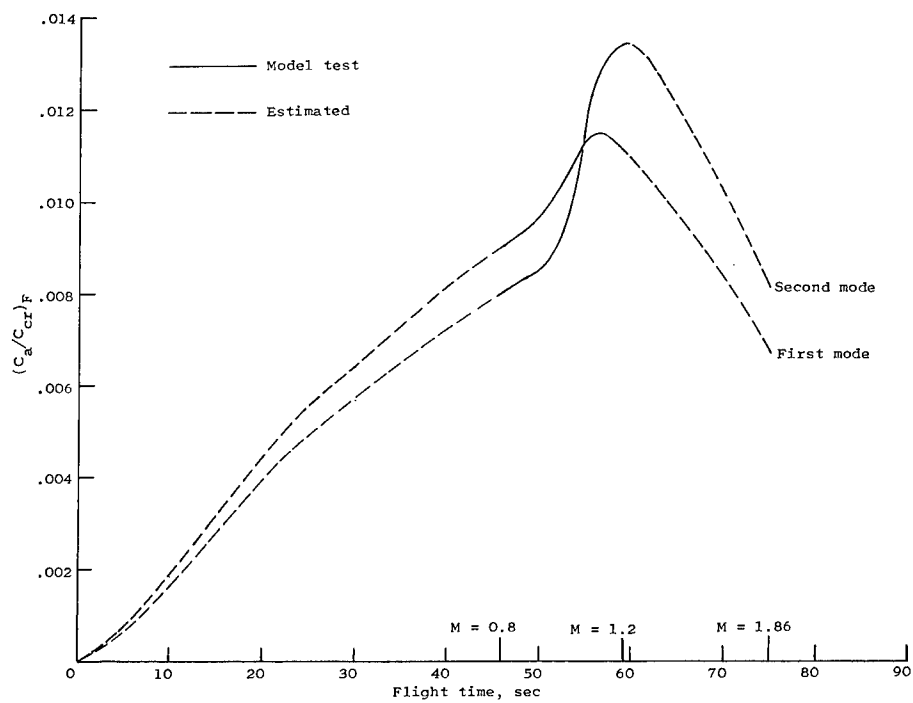


(c) Jupiter nose cone configurations.

Figure 11.- Concluded.

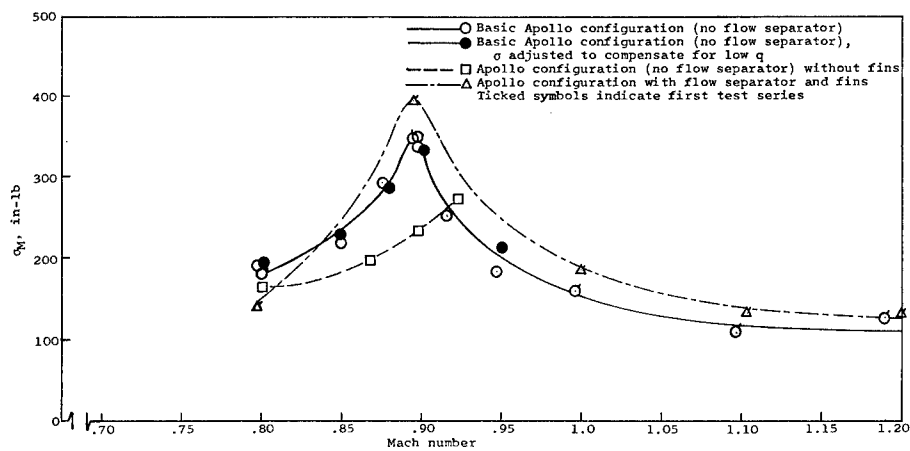


(a) Basic Apollo configuration.

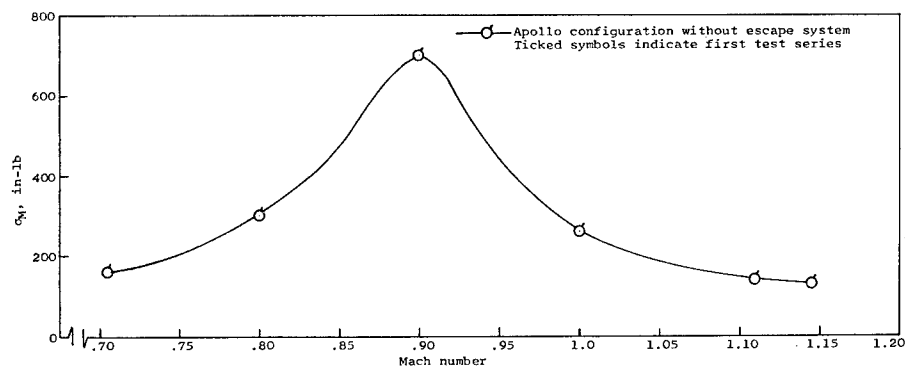


(b) Jupiter nose cone configuration.

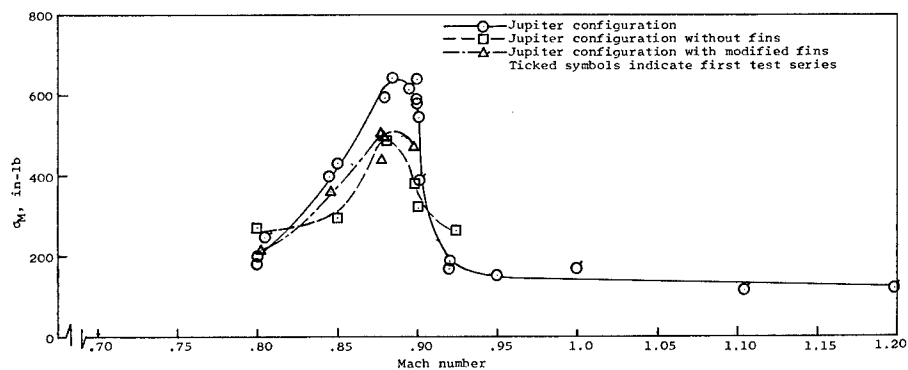
Figure 12.- Variation with time along launch trajectory of the ratio of aerodynamic damping to critical damping for the flexible vibration modes at $\alpha = 0^\circ$.



(a) Apollo configurations with escape system.

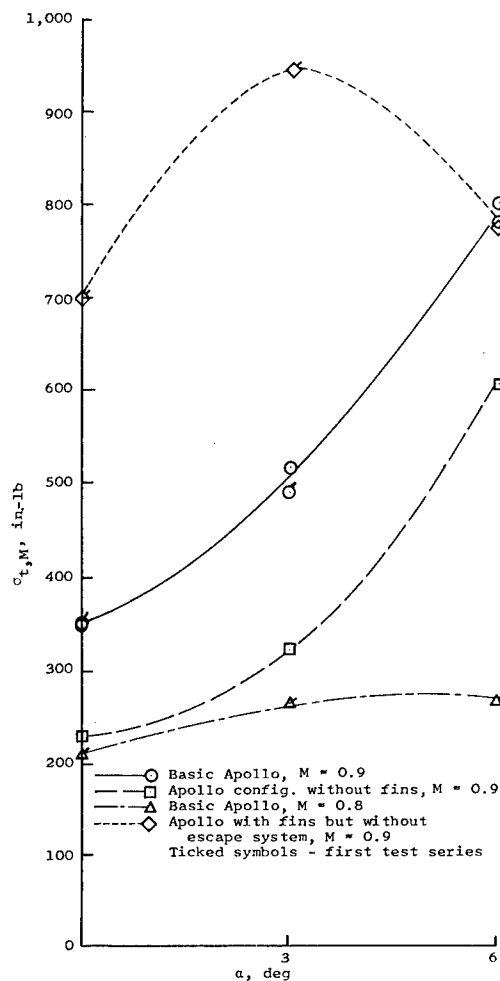


(b) Apollo configuration without escape system.

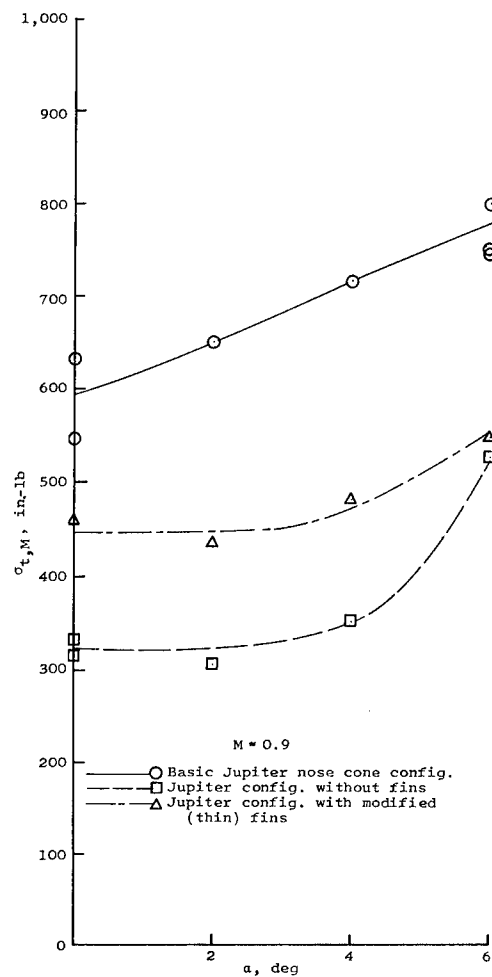


(c) Jupiter nose cone configurations.

Figure 13.- Effect of configuration changes on variation of model root-mean-square bending moment at model station 73.5 inches with Mach number for $\alpha = 0^\circ$.



(a) Apollo configurations.



(b) Jupiter nose cone configurations.

Figure 14.- Effect of angle of attack on variation of model total root-mean-square bending moment at model station 73.5 inches for various configurations.

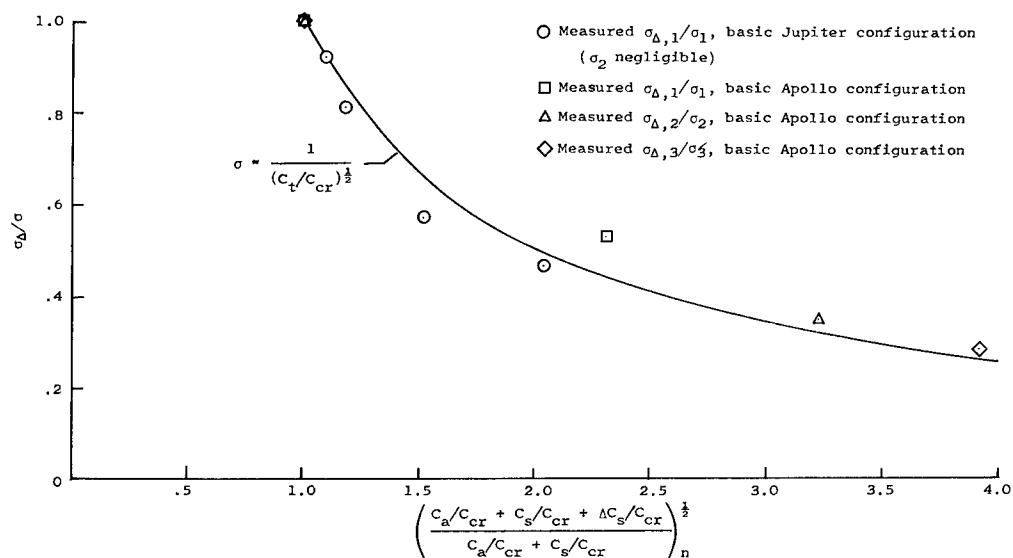
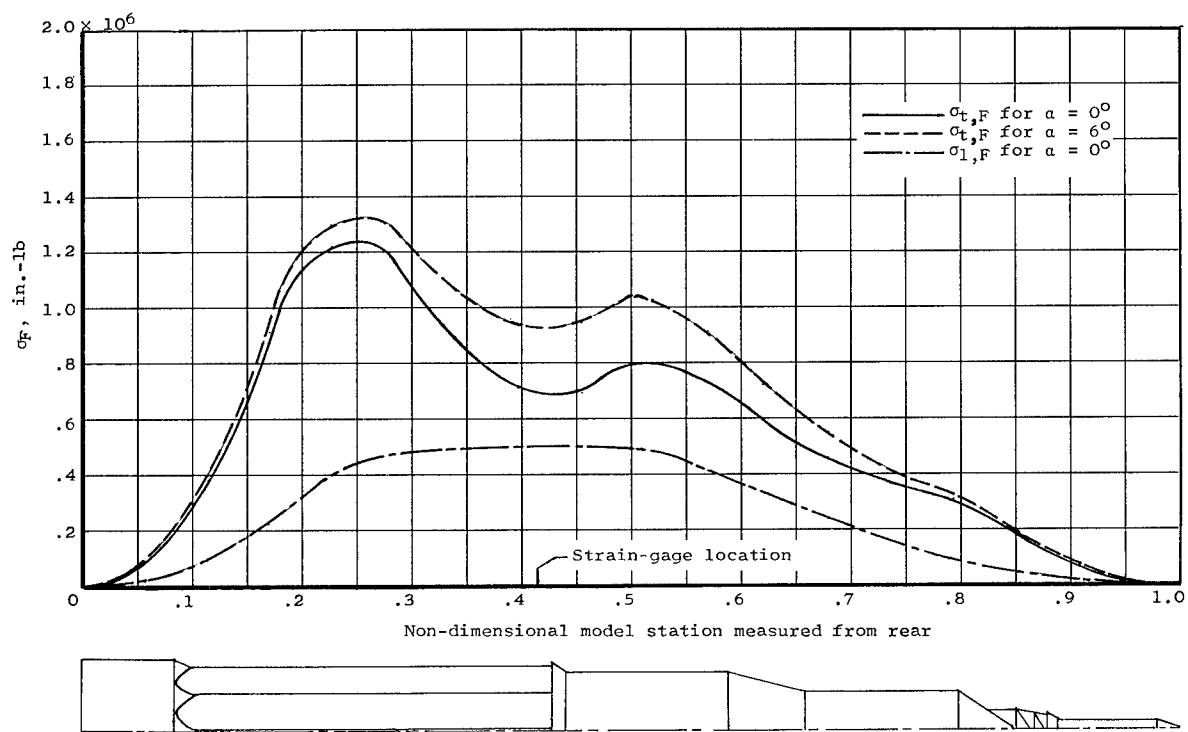
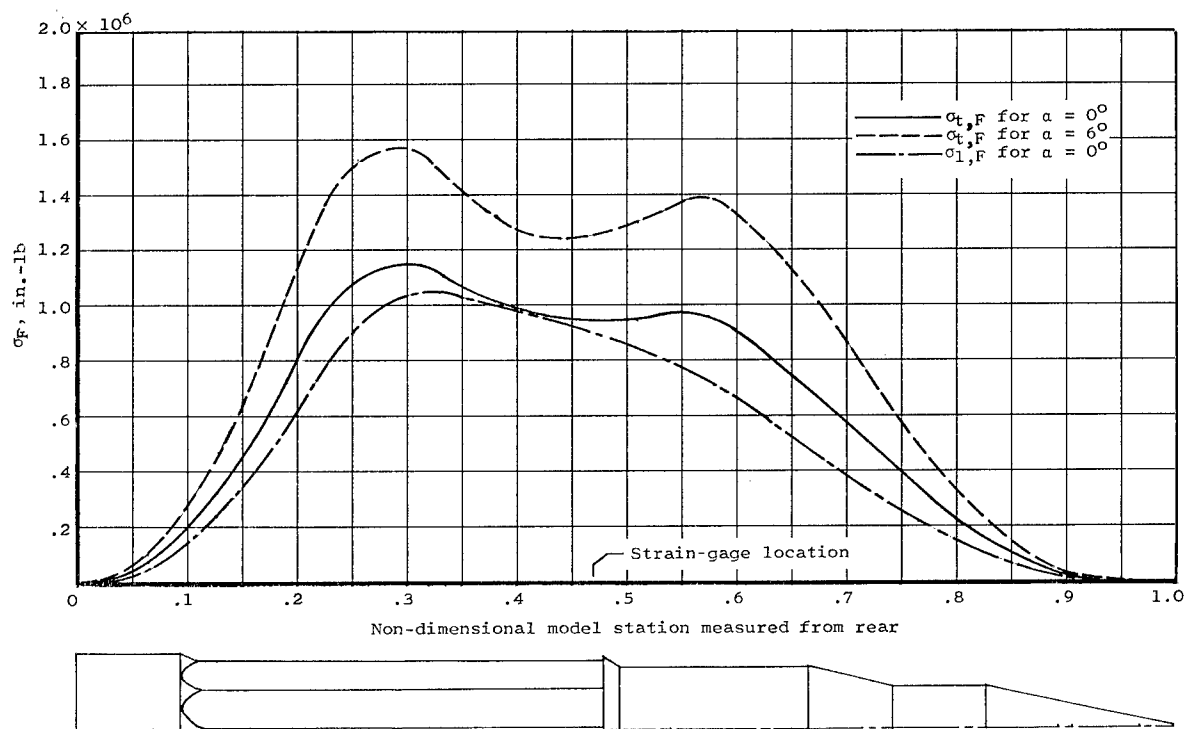


Figure 15.- Effect of increase in structural damping on model buffet response at $M = 0.9$, $\alpha = 0^\circ$.



(a) Basic Apollo configuration (without flow separator).



(b) Basic Jupiter nose cone configuration.

Figure 16.- Total full-scale root-mean-square bending-moment distributions. $M = 0.9$.

"The aeronautical and space activities of the United States shall be conducted so as to contribute . . . to the expansion of human knowledge of phenomena in the atmosphere and space. The Administration shall provide for the widest practicable and appropriate dissemination of information concerning its activities and the results thereof."

—NATIONAL AERONAUTICS AND SPACE ACT OF 1958

NASA SCIENTIFIC AND TECHNICAL PUBLICATIONS

TECHNICAL REPORTS: Scientific and technical information considered important, complete, and a lasting contribution to existing knowledge.

TECHNICAL NOTES: Information less broad in scope but nevertheless of importance as a contribution to existing knowledge.

TECHNICAL MEMORANDUMS: Information receiving limited distribution because of preliminary data, security classification, or other reasons.

CONTRACTOR REPORTS: Technical information generated in connection with a NASA contract or grant and released under NASA auspices.

TECHNICAL TRANSLATIONS: Information published in a foreign language considered to merit NASA distribution in English.

TECHNICAL REPRINTS: Information derived from NASA activities and initially published in the form of journal articles.

SPECIAL PUBLICATIONS: Information derived from or of value to NASA activities but not necessarily reporting the results of individual NASA-programmed scientific efforts. Publications include conference proceedings, monographs, data compilations, handbooks, sourcebooks, and special bibliographies.

Details on the availability of these publications may be obtained from:

SCIENTIFIC AND TECHNICAL INFORMATION DIVISION
NATIONAL AERONAUTICS AND SPACE ADMINISTRATION
Washington, D.C. 20546